Cell Reports

Article

Vitamin D receptor, STAT3, and TET2 cooperate to establish tolerogenesis

Graphical abstract

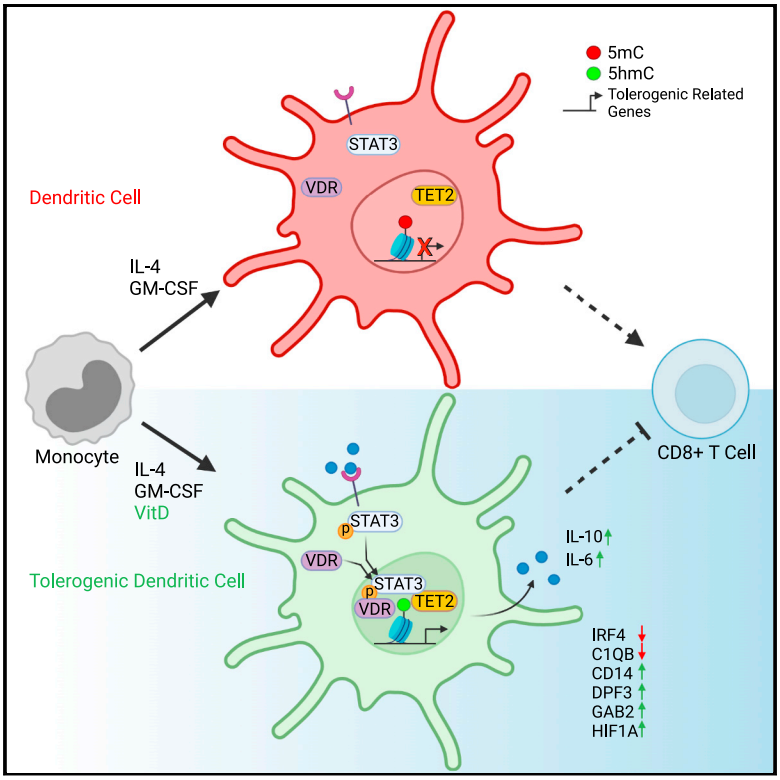

Highlights

- Vitamin D induces DNA demethylation at VDR binding sites in dendritic cells (DCs)
- Differentiation to tolerogenic DCs associates with IL-6-JAK-STAT3 pathway activation
- VDR, STAT3, and TET2 interact with each other in tolerogenic DCs
- Pharmacological inhibition of JAK2 reverts vitamin D-induced DC tolerogenesis

Authors

Francesc Català-Moll, Anna G. Ferreté-Bonastre, Gerard Godoy-Tena, ..., Javier Rodríguez-Ubreva, Tianlu Li, Esteban Ballestar

Correspondence

eballestar@carrerasresearch.org

In brief

Català-Moll et al. show that vitamin D induces DNA demethylation and transcriptional activation at VDR binding sites, as well as IL-6-JAK-STAT3 pathway activation associated with acquisition of tolerogenesis by dendritic cells. VDR, STAT3, and TET2 interact with each other. Pharmacological inhibition of JAK2 reverts vitamin D-induced tolerogenic properties of DCs.

Català-Moll et al., 2022, Cell Reports *38*, 110244
January 18, 2022
https://doi.org/10.1016/j.celrep.2021.110244

CellPress

Cell Reports

CellPress
OPEN ACCESS

Article

Vitamin D receptor, STAT3, and TET2 cooperate to establish tolerogenesis

Francesc Català-Moll,[1,4] Anna G. Ferreté-Bonastre,[1,4] Gerard Godoy-Tena,[1,4] Octavio Morante-Palacios,[1] Laura Ciudad,[1] Laura Barberà,[1] Federico Fondelli,[2,3] Eva M. Martínez-Cáceres,[2,3] Javier Rodríguez-Ubreva,[1] Tianlu Li,[1,4] and Esteban Ballestar[1,5,*]

[1]Epigenetics and Immune Disease Group, Josep Carreras Research Institute (IJC), Badalona, 08916 Barcelona, Spain
[2]Division of Immunology, Germans Trias i Pujol Hospital, LCMN, Germans Trias i Pujol Research Institute (IGTP), Badalona, 08916 Barcelona, Spain
[3]Department of Cell Biology, Physiology, Immunology, Autonomous University of Barcelona, Bellaterra, 08193 Barcelona, Spain
[4]These authors contributed equally
[5]Lead contact
*Correspondence: eballestar@carrerasresearch.org
https://doi.org/10.1016/j.celrep.2021.110244

SUMMARY

The active form of vitamin D, 1,25-dihydroxyvitamin D3, induces a stable tolerogenic phenotype in dendritic cells (DCs). This process involves the vitamin D receptor (VDR), which translocates to the nucleus, binds its cognate genomic sites, and promotes epigenetic and transcriptional remodeling. In this study, we report the occurrence of vitamin D-specific DNA demethylation and transcriptional activation at VDR binding sites associated with the acquisition of tolerogenesis *in vitro*. Differentiation to tolerogenic DCs associates with activation of the IL-6-JAK-STAT3 pathway. We show that JAK2-mediated STAT3 phosphorylation is specific to vitamin D stimulation. VDR and the phosphorylated form of STAT3 interact with each other to form a complex with methylcytosine dioxygenase TET2. Most importantly, pharmacological inhibition of JAK2 reverts vitamin D-induced tolerogenic properties of DCs. This interplay among VDR, STAT3, and TET2 opens up possibilities for modulating DC immunogenic properties in clinics.

INTRODUCTION

Dendritic cells (DCs) are a heterogeneous group of innate immune cells that have a key role in initiating adaptive responses. Also, DCs are not only central for coordinating immune responses against a threat but also needed to regulate the immune system at steady state and for inducing immune tolerance (Morante-Palacios et al., 2021). Like in other myeloid cell populations, the immunological properties of DCs vary with the environment. In general, terminal myeloid cell differentiation is highly dependent on the activation of specific signaling pathways in response to extracellular signals, such as inflammatory cytokines, hormones, vitamins, and other factors (Álvarez-Errico et al., 2015), which determine the immunogenicity of the resulting myeloid cells. The activation of signaling pathways leads to the activation of specific sets of transcription factors (TFs). Sequence-specific DNA binding of TFs is a pivotal process for establishing gene expression patterns in concert with the epigenetic machinery that determines cell identity and function (Monticelli and Natoli, 2017). Recent evidence has shown that several TFs are associated with DNA demethylation to increase genomic accessibility of their binding genomic regions, thus facilitating the binding of subsequent TFs (Mahé et al., 2017). In this regard, methylcytosine dioxygenase ten-eleven translocation (TET2), the most relevant enzyme involved in active DNA demethylation in the myeloid compartment, can interact with a variety of TFs, such as PU.1, C/EBPα, KLF4, and others, in order to facilitate their recruitment to different genomic regions (Costa et al., 2013; Guilhamon et al., 2013; de la Rica et al., 2013; Lio et al., 2016; Mendes et al., 2021; Sardina et al., 2018; Wang et al., 2015; Xiong et al., 2016). Recently, it has been demonstrated that TET2 mutations, which are frequent in myeloid leukemias, lead to DNA hypermethylation of enhancer regions and changes in the subsequent binding of TFs, particularly members of the basic helix-loop-helix (bHLH) TF family (Rasmussen et al., 2019). This suggests that TET2 recruitment by TFs leads to epigenetic remodeling that facilitates the binding of subsequent TFs (Rasmussen et al., 2019). Moreover, a reciprocal relationship between DNA methylation and histone modifications has long been established. TET2 has been not only described to modulate trimethylation of K4 of histone H3 (H3K4me3) (Deplus et al., 2013), a mark of active transcription, but also shown to coordinate trimethylation of K27 of histone H3 (H3K27me3), a mark of heterochromatin, in an inverse manner (Ichiyama et al., 2015).

Calcitriol (1,25-dihydroxyvitamin D3), the active form of vitamin D3 (henceforth referred to as vitamin D), is a major modulator of the immune system (Barragan et al., 2015; Carlberg, 2019; Mora et al., 2008). DCs are the most susceptible cell type to vitamin D in a mixed immune population (Mora et al., 2008). In these cells, vitamin D can generate a stable maturation-resistant tolerogenic

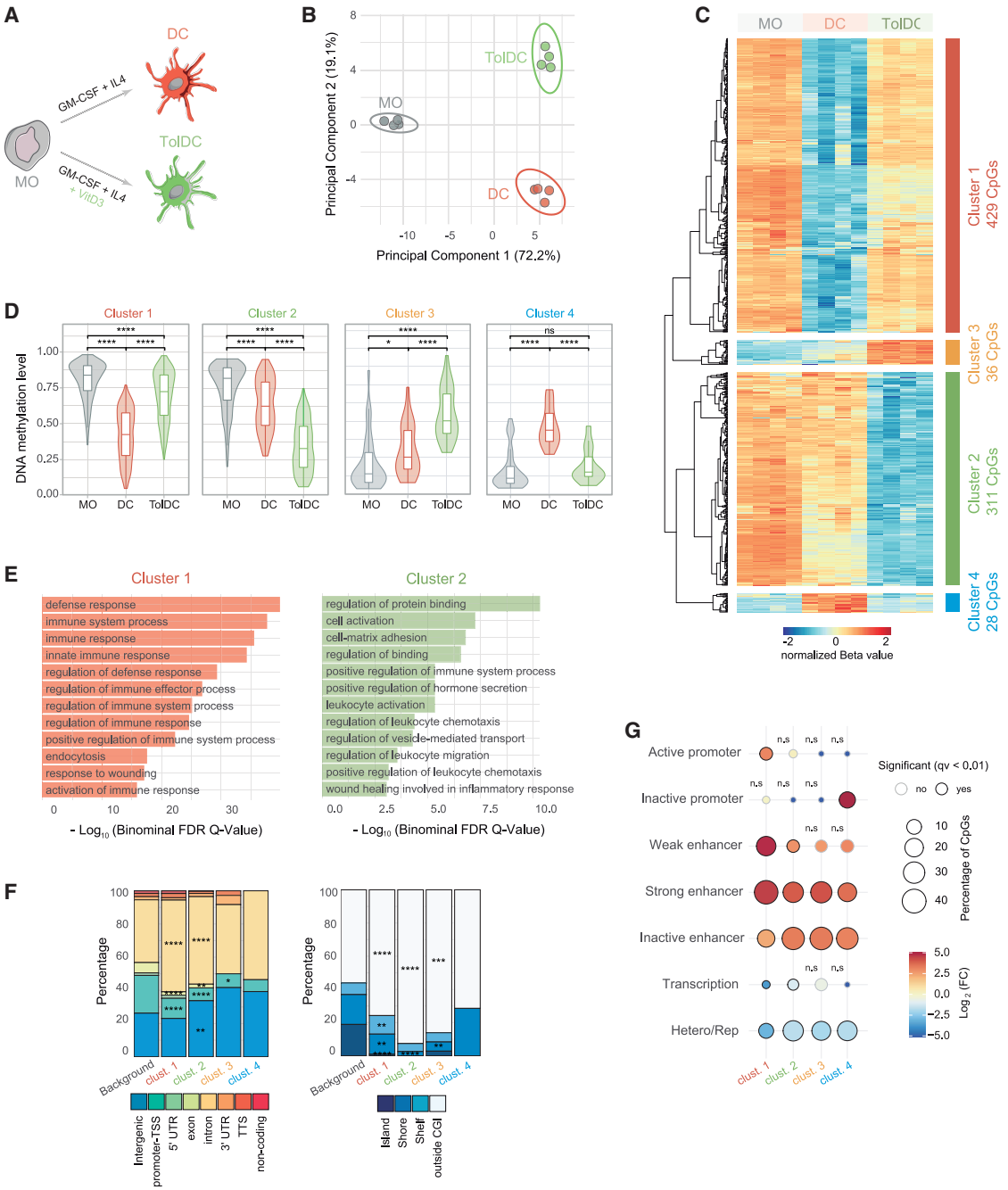

Figure 1. DNA methylation dynamics throughout vitamin D-exposed dendritic-cell differentiation (n = 4, two independent experiments)

(A) Schematic overview of the differentiation model from human peripheral blood MOs to DCs and TolDCs.

(B) Principal-component analysis of differentially methylated CpGs.

(C) DNA methylation heatmap and cluster analysis of four paired samples of MOs and their derived DCs and TolDCs at day 5 of differentiation. The heatmap includes all CpG-containing probes displaying significant methylation changes (differential beta value ≥ 0.2 and q value < 0.05) only in the TolDC-DC comparison. The color annotation of the lateral bar represents the membership to cluster 1 in red (DC-specific DNA demethylation), cluster 2 in green (TolDC-specific DNA demethylation), cluster 3 in orange (TolDC-specific DNA hypermethylation), and cluster 4 in blue (DC-specific DNA hypermethylation).

(D) Box and violin plots summarizing the distribution of DNA methylation levels per cell type and cluster.

(E) Gene ontology (GO) terms associated with CpGs from cluster 1 (red) and cluster 2 (green) as analyzed by GREAT software. Bars represent log-transformed binomial q values of the GO term enrichment.

(F) Location proportions of CpGs from each cluster in the context of CpG islands (CGIs) (right) and gene-related regions (left).

(legend continued on next page)

phenotype *in vitro*, with a low level of expression of immunogenic molecules, such as HLA-DR, CD80, and CD86, and increased interleukin (IL)-10/IL-12p70 ratios that are maintained even after removal of the compound (Van Halteren et al., 2002). After ligand recognition, vitamin D receptor (VDR) translocates to the nucleus and acts not only as a TF, controlling the expression of a set of immune and metabolic genes (Carlberg, 2019; Ferreira et al., 2013), but also as a repressor of nuclear factor kappa-light-chain-enhancer of activated B cells (NF-kB) at different levels (Carlberg, 2019; Fetahu et al., 2014). Several studies have shown the capacity of VDR to interact with a range of TFs, including PU.1 and GABPA, and with chromatin remodeling and histone modification enzymes, such as BRD7 and KDM6B (Pereira et al., 2011; Seuter et al., 2017, 2018; Wei et al., 2018). Previous work has shown that vitamin D may induce DNA methylation changes in myeloid cells (Ong et al., 2021). However, the molecular mechanism that leads to the acquisition of differential methylation patterns remains unexplored.

Vitamin D supplementation is generally used as a preventive agent or a co-adjuvant for diseases with underlying autoimmune or pro-inflammatory states (Bscheider and Butcher, 2016; Dankers et al., 2017). DCs represent an excellent target of vitamin D to dampen autoimmunity and inflammation, not only because these myeloid cells express the whole set of enzymes to generate the active form of vitamin D (Mora et al., 2008) but also because of their unique role as initiators of immune responses. However, the role of DCs in vitamin D-mediated immunomodulation is not fully understood. In addition, DCs with tolerogenic function (TolDCs) have become a promising immunotherapeutic tool for reinstating immune tolerance in autoimmune diseases and in allogeneic bone marrow and solid organ transplantation (Morante-Palacios et al., 2021). The stability of the tolerogenic phenotype suggests that regulatory mechanisms that allow the maintenance of stable changes of gene expression are involved. In this sense, DNA methylation is a major epigenetic modification closely involved in the acquisition or stabilization of transcriptional states (Luo et al., 2018). Peripheral blood monocyte (MO)-derived DCs represent a useful model for studying the properties of DCs. It has been previously described that DCs differentiated from isolated MOs by the addition of granulocyte-macrophage colony-stimulating factor (GM-CSF) and IL-4 *in vitro* closely resemble CD1c$^+$ DCs at the transcriptional level (Goudot et al., 2017). Exposure of MO-derived DCs to vitamin D results in the inhibition of differentiation and maturation into potent antigen-presenting cells and gain in the capacity to inhibit T cell proliferation (Piemonti et al., 2000). Similarly, CD1c$^+$ DCs cultured *in vitro* with vitamin D for 2 days acquire a typical semi-mature phenotype after exposure to a DC maturation cocktail, with low CD83 expression, and a tolerogenic phenotype, as they suppressed alloimmunity *in vivo*, in a mouse model (Chu et al., 2012).

In this study, we studied epigenetic determinants critical for the acquisition of tolerogenic properties during *in vitro* human MO-derived DC differentiation in the presence of vitamin D. We demonstrate an interplay between VDR and the Janus kinase (JAK) 2/signal transducer and activator of transcription (STAT) 3 pathway associated with the generation of a specific TET-dependent DNA demethylation signature in TolDCs. It involves a direct physical interaction between VDR, STAT3, and TET2 that leads to the acquisition and stabilization of the tolerogenic properties of DCs in the presence of vitamin D.

RESULTS

Vitamin D induces the acquisition of a specific DNA methylation profile associated with tolerogenesis during *in vitro* DC differentiation

To investigate the effects of vitamin D in DNA methylation during the acquisition of tolerogenic properties by DCs, we first differentiated *in vitro* peripheral blood MOs from human donors to DCs and TolDCs for 6 days using GM-CSF and IL-4 in the absence and presence of vitamin D, respectively (Figure 1A). As previously described (Penna and Adorini, 2000; Piemonti et al., 2000), TolDCs had higher levels of the surface markers CD14 and CD11b and lower levels of HLA-DR, CD1a, and CD86 than did DCs (Figure S1A). To confirm the resemblance between our *in vitro* model with *in vivo* DCs, we integrated the expression profiles of MOs, DCs (12 h and 120 h), and TolDCs (12 h and 120 h) (Széles et al., 2009) with previously published expression datasets (Goudot et al., 2017; Segura et al., 2013) from MOs, *in vitro*-derived DCs and macrophages (MACs), and *in vivo* DCs and MACs. According to t-distributed stochastic neighbor embedding (t-SNE) analysis, TolDCs (differentiated in the presence of vitamin D), among different DC subsets, are the ones nearer different MAC types with immunosuppressive phenotypes (Figure S1B).

In concordance with previous studies (Piemonti et al., 2000), we observed that TolDCs were able to inhibit CD8$^+$ T cell proliferation *in vitro*, in contrast to DCs, confirming their immunosuppressive properties (Figure S1C). Furthermore, we also observed increased levels of VDR in the nucleus following vitamin D exposure, in agreement with previous studies, suggesting that VDR preferentially acts in the nucleus (Figure S1D). Altogether, our results confirmed the validity of this *in vitro* model to generate and study TolDCs by the involvement of VDR through vitamin D exposure.

We then obtained and compared the DNA methylation profiles of MOs, DCs, and TolDCs using BeadChip arrays (see STAR Methods), which interrogate the methylation status of >850,000 CpG positions across the entire genome, covering 99% of the reference sequence genes. Principal-component analysis (PCA) showed that most of the variability observed at the DNA methylation level may be explained by events common to the two differentiation processes (principal component 1;

(G) Bubble chart depicting the enrichment (red) or depletion (blue) of the CpGs from each cluster in the chromatin states from DCs (Pacis et al., 2015). The circle filling color represents the logarithmic value of the ratio between the percentage of CpGs with the feature in each cluster and the percentage of CpGs with the feature in the background. Circle size indicates the percentage of CpGs from each cluster in the chromatin state, and the circle edge indicates the statistical significance of the enrichment (black: significant; no edge: not significant; q value < 0.01).
Statistical tests: paired two-tailed t test (D), Pearson correlation (E), and two-tailed Fisher's exact test (F and G) (*p < 0.05; **p < 0.01; ***p < 0.001; ****p < 0.0001, ns = not significant). FDR, false discovery rate.

Figure 1B). However, the second principal component is capable of clustering DCs and TolDCs separately (Figure 1B). Differentiation mainly resulted in DNA demethylation in which there were both condition-specific demethylation events and demethylation events common to both differentiation processes (Figure S1E). A small proportion of DNA methylation changes was attributed to gains of DNA methylation during differentiation (Figure S1E). Hierarchical clustering of differentially methylated CpGs between DCs and TolDCs (adjusted $p < 0.05$ and absolute differential beta ≥ 0.2) revealed four main groups of CpG sites (Figures 1C and 1D and Table S1): a group of CpGs that underwent specific demethylation in DCs (cluster 1: 429 CpGs); a second group that was specifically demethylated in TolDCs (cluster 2: 311 CpGs); another group that gained methylation in TolDCs (cluster 3: 36 CpGs); and finally a group of CpGs with DC-specific gains in DNA methylation (cluster 4: 28 CpGs).

To confirm these observations in the context of *in vivo* circulating DCs, we obtained the DNA methylation profiles of whole blood-isolated cDCs ($CD1c^+$ DCs) cultured in the absence and presence of vitamin D for 3 days and observed that, similar to TolDCs generated *in vitro*, cDCs exposed to vitamin D underwent DNA demethylation in cluster 2 CpGs (Figure S1F). This confirmed that demethylation observed in cluster 2 CpGs were specific to vitamin D exposure.

Functional gene ontology (GO) analysis revealed that CpGs in cluster 1 are associated with immunological categories, such as defense and immune response, whereas those in cluster 2 are more highly enriched in cell activation, positive regulation of immune system process, and wound healing involved in inflammatory response (Figure 1E). For clusters 3 and 4, GO analysis did not show enrichment in any functional categories, probably due to their small size. In all clusters, the majority of changes occurred in introns and intergenic regions with underrepresentation of promoter-transcriptional start sites (TSSs). However, whereas cluster 1 exhibited a marked enrichment of intronic regions with respect to background, the other clusters were enriched in both intronic and intergenic locations (Figure 1F, left). Concordantly, CpGs of all clusters were observed to be located outside of CpG islands, particularly for cluster 2 (Figure 1F, right). Next, we mapped the chromatin states of the CpG sites undergoing changes in methylation in the four clusters using chromatin segmentation data generated in DCs (Pacis et al., 2015) (Figure 1G). We observed an enrichment in enhancer regions for all clusters and an enrichment for inactive promoters for cluster 4. Moreover, cluster 1 (DC-specific demethylation) was enriched in weak (H3K27ac + H3K4me1 + H3K4me3) and strong (H3K27ac + H3K4me1) enhancers, while cluster 2 (TolDC-specific demethylation) was more enriched in inactive enhancers (H3K4me1) in DCs, suggesting that these inactive regions in DCs are activated in TolDCs. In all, our results indicated that vitamin D-driven demethylation events occurred in regions that may play important roles in regulating gene expression and establishing the tolerogenic phenotype of TolDCs.

DNA demethylation in TolDCs is an active process and is associated with changes in gene expression

DNA methylation has long been established to influence gene expression (Jones, 2012), although the dynamics are complex and highly dependent on genomic location. CpGs that underwent TolDC-specific DNA demethylation during differentiation were largely situated in open seas corresponding to enhancers; hence, it is plausible to envision that they control gene expression, which results in the final tolerogenic phenotype. We therefore integrated our DNA methylation dataset with publicly available expression data generated in the same *in vitro* models (Széles et al., 2009). We observed a significant inverse relationship between levels of DNA methylation and mRNA expression at 12 h ($r = -0.5926$; $p = 4.90e\text{-}14$) and 5 days of differentiation ($r = -0.4108$; $p = 4.57e\text{-}11$) (Figure 2A). Furthermore, dividing cluster 1 and 2 CpGs based on their genomic location in relation to previously identified enhancer regions (Pacis et al., 2015), we observed that genes associated with cluster 1 CpGs located at active enhancers of DCs displayed higher expression levels in DCs than in TolDCs (Figure 2B).

To explore the dynamics of the relationship between DC- (cluster 1) and TolDC-specific demethylation (cluster 2), we performed bisulfite pyrosequencing and qRT-PCR in a selected group of genes of a set of samples over time. A few genes from each cluster were selected for further analysis based on the conditions that they had the maximum possible difference in DNA methylation during differentiation within their corresponding cluster, that they were differentially expressed, and that there were previous reports relating them with relevant immune properties. For instance, from cluster 1, we chose *IRF4* and *C1QB*, which are important for normal DC differentiation from MOs (Teh et al., 2011; Murphy et al., 2016), and from cluster 2, *CD14* and *DPF3* were selected for being specific markers of TolDCs and being involved in DC chemotaxis, respectively (Liu et al., 2019; Torres-Aguilar et al., 2010). Bisulfite pyrosequencing of these genes showed a high concordance ($r = 0.978$; $p < 2.2 \times 10^{-16}$) with the data obtained from the EPIC arrays (Figure 2C). DC-specific (cluster 1) genes, such as *IRF4* and *C1QB*, were upregulated in DCs in parallel with their specific DNA demethylation (Figure 2D). Similarly, for TolDC-specific (cluster 2) genes, such as *CD14* and *DPF3*, transcript upregulation occurred only in TolDCs in parallel with their corresponding DNA demethylation (Figure 2E). In agreement with previous reports, stimulus-induced DNA demethylation occurred succeeding specific gene expression changes (Pacis et al., 2019). In all, our results suggested that vitamin D-driven DNA demethylation occurred in association with upregulation of TolDC-specific genes.

To further characterize the mechanisms driving DNA demethylation during MO-to-DC and MO-to-TolDC differentiation, we next investigated whether the demethylation was due to active demethylation or replication-mediated passive demethylation. Utilizing BrdU proliferation assay, no proliferation was observed in DCs and TolDCs up to 6 days of differentiation (Figure S2A); hence, all DNA demethylation events observed were driven by active demethylation. In this regard, we and others have previously shown that loss of methylation in terminal differentiation from MOs is accompanied by a transient increase in 5-hydroxymethylcytosine (5hmC) and involves the participation of TET2 methylcytosine dioxygenase (Garcia-Gomez et al., 2017; Klug et al., 2013). We then determined the 5hmC levels of CpGs that became demethylated during DC and TolDC differentiation and observed that there was indeed a gain of 5hmC in these

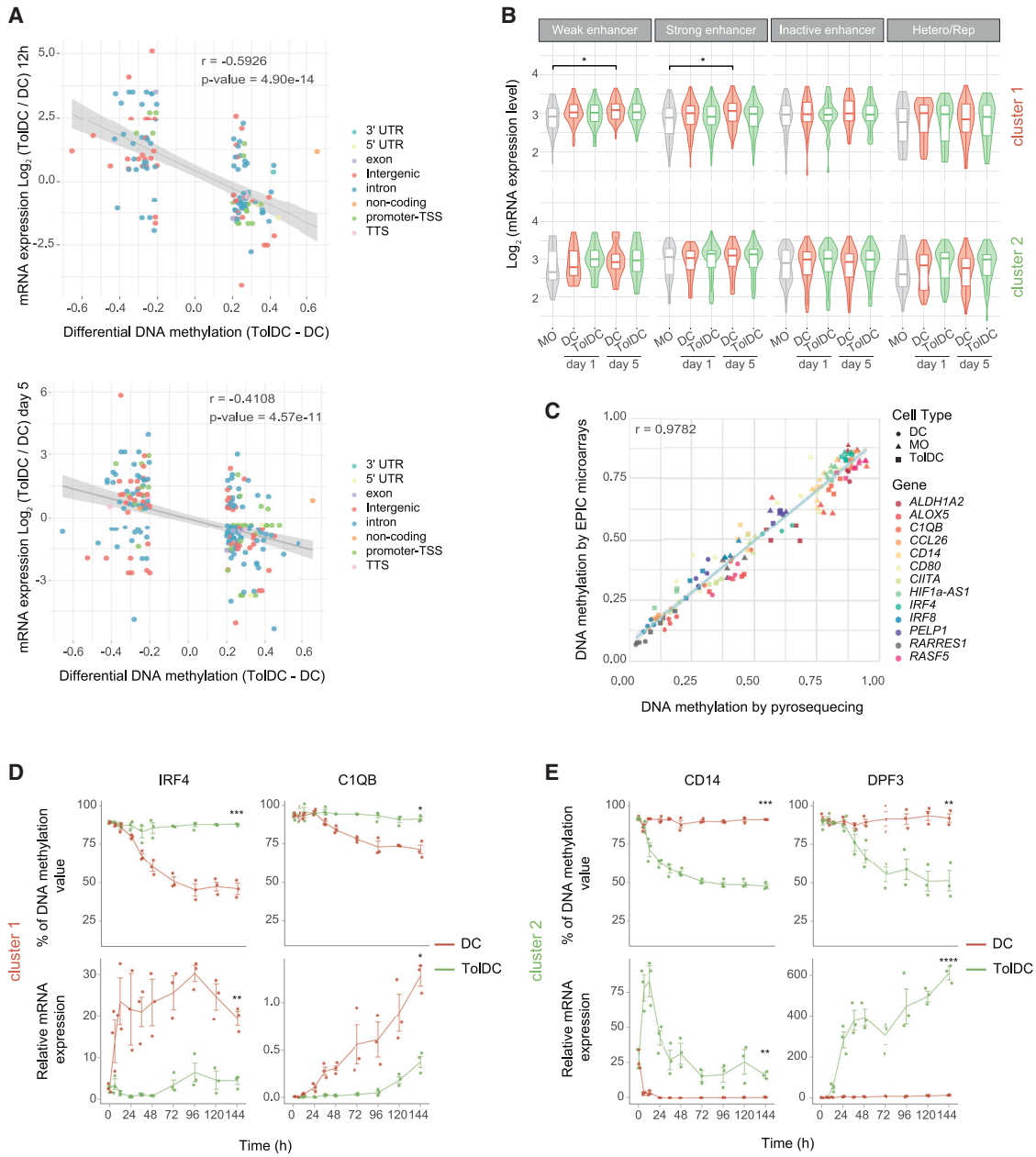

Figure 2. Integration of gene expression with DNA methylation

(A) Scatter plot showing the correlation between DNA methylation differences and gene expression changes between DCs and TolDCs at 12 h (top) and day 5 (bottom) of differentiation. Only differentially methylated CpGs are represented. Dot color indicates gene-related associations.

(B) Box and violin plots summarizing the mRNA expression levels per cell type of genes annotated to CpGs from cluster 1 (top) and cluster 2 (bottom) divided by chromatin state annotation of the associated CpG. Adjustment for multiple comparisons was performed with false discovery rate.

(C) Scatter plot showing the correlation between methylation array values and bisulfite pyrosequencing DNA methylation values (n = 4, two independent experiments).

(D) DNA methylation (top) and mRNA expression (bottom) kinetics of two representative examples of cluster 1 genes. CpGs studied include cg10630015 (IRF4) and cg04097715 (C1QB) (n = 3, one single experiment).

(E) DNA methylation (top) and mRNA expression (bottom) kinetics of two representative examples of cluster 2 genes (n = 3, two independent experiments). CpGs studied include cg05620710 (CD14) and cg25205844 (DPF3).

Statistical tests: Pearson correlation (A) and unpaired two-tailed t test (B, D, and E) (*p < 0.05; **p < 0.01; ***p < 0.001; ****p < 0.0001).

CpGs (Figure S2B). Finally, utilizing publicly available DNase-sequencing (seq) datasets from MOs (Feingold et al., 2004), we observed that more than 75% of cluster 2 CpGs corresponded to closed chromatin in MOs (Figure S2C), which reinforced the hypothesis that DNA demethylation was mediated by an active event. Altogether, our results suggested that specific active DNA demethylation following vitamin D exposure is mediated through methylcytosine dioxygenase activity, most likely associated with TET2.

VDR binding is associated with DNA demethylation and active chromatin during MO-to-TolDC differentiation

In concordance with previous work (Jakob et al., 1992), we observed that exposure to vitamin D during DC differentiation increased the nuclear levels of VDR (Figure S1D). Hence, it is plausible that liganded VDR plays a direct role in driving DNA demethylation following vitamin D exposure during TolDC differentiation. Hence, we performed chromatin immunoprecipitation (ChIP)-seq analysis of VDR in DCs and TolDCs. First, we observed that exposure to vitamin D during TolDC differentiation led to a sharp increase in overall VDR genomic binding (Figures 3A and 3B).

Interestingly, motif discovery analysis revealed promiscuity of VDR with respect to its genomic binding preferences, with only 37% of regions having the canonical VDR binding motif (Figure 3C), which suggests the cooperation of VDR with other TFs during TolDC differentiation. Second, functional annotation of VDR-bound genes revealed enrichment of immune- and signaling-related categories, such as myeloid and granulocyte activations and cytokine receptor activity (Figure 3D). In fact, several genes previously described to be related to the tolerogenic properties of TolDCs, such as *IL10*, *ANXA1*, and *CD163* (Navarro-Barriuso et al., 2018), are direct targets of VDR (Table S2). Third, global inspection of VDR genomic occupancy showed that VDR preferentially binds to promoters and introns in comparison with background (Figure 3E, left). We also observed enrichment of VDR binding in CpG islands, shores, and shelves, which was compatible with the enrichment noted in promoters (Figure 3E, right). Annotation of VDR peaks in relation to previously published data of DC chromatin states (Pacis et al., 2015) showed the preference of VDR for binding regions that correspond to promoters and enhancers in DCs (Figure 3F).

To further characterize the relationship between VDR and DNA methylation, we overlapped our generated DNA methylation data with VDR ChIP-seq data and observed a specific enrichment of VDR binding in TolDCs to CpGs that became demethylated in TolDCs (cluster 2), and this was not observed for the other clusters (Figures 4A, 4B, and S3A). In fact, we observed that over 40% of CpG sites in cluster 2 had significant VDR binding (Figure 4C). For instance, cluster 2 CpGs mapped to genes, such as *GAB2* and *HIF1A*, situated within the binding peaks of VDR in TolDCs (Figure 4D) and located in closed chromatin regions in MOs (Figure S3B). These genes are of particular interest because GAB2 has been implicated in phosphatidylinositol 3-kinase (PI3K) pathway activation (Pratt et al., 2000), a pathway implicated in DC tolerogenesis (Ferreira et al., 2015). Furthermore, hypoxia-inducible factor 1-alpha (HIF1A) is a key factor for the tolerogenic properties of myeloid-derived suppressor cells (MDSCs) in the tumor microenvironment (Corzo et al., 2010). The dynamics of DNA methylation and gene expression of these two genes confirmed specific DNA demethylation in TolDC, and differential gene expression changes in relation to DCs (Figures 4E and 4F).

As indicated in the introduction, TET-mediated demethylation is associated with histone modifications, such as H3K4me3 (Deplus et al., 2013) and H3K27me3 (Ichiyama et al., 2015). Hence, we speculated that changes in DNA methylation were accompanied by changes in histone modifications, and their dynamics might be associated with VDR recruitment following vitamin D exposure. Therefore, we performed ChIP-qPRC of VDR together with these activating (H3K4me3) and repressive (H3K27me3) histone modifications. We also added an antibody against H3 acetylation (H3ac), characteristic of active chromatin. To discriminate between the effects of a tolerogenic phenotype acquired through a 6-day differentiation and the effects directly caused by the presence of vitamin D in the medium, we performed ChIPs in MOs, DCs, TolDCs, and also DCs treated with vitamin D for 30 min (DC + vitD). First, we observed a significant increase in VDR binding (Figure 4G) in DCs treated with vitamin D and in TolDCs. Second, in the aforementioned cluster 2 genes *GAB2* and *HIF1A*, we only observed a significant increase, associated with VDR binding, for H3ac (Figure 4G). This finding was extendable to other cluster 2 genes, such as *HOPX*, *IL6*, *INHBA*, and *LYRM1* (Figure S3C).

Hence, altogether, our data suggested the coordination between VDR binding, specific DNA demethylation, changes in histone H3 acetylation, and gene expression upregulation in TolDC differentiation.

Differentiation to DCs in the presence of vitamin D associates with activation of IL-6-JAK-STAT3 signaling pathway, and both VDR and STAT3 interact with TET2

Vitamin D, through its receptor VDR, induces changes in cytokine production and a profound metabolic reprogramming in human DC (Ferreira et al., 2015). For this reason, we hypothesized that autocrine/paracrine activation of secondary signaling pathways during differentiation could lead to the activation of a set of TFs downstream to VDR that could be relevant to TolDC differentiation. To explore this possibility, we adapted a tool initially designed to explore intercellular communication in bulk and single-cell expression data to test autocrine/paracrine signal activation (Browaeys et al., 2020). Note that our differentiation model does not allow to distinguish between autocrine or paracrine activation. With this approach, and using genes associated with both demethylation clusters with significant expression differences (fold-change <0.5 or >2, and adjusted $p < 0.05$) as input, we inferred potential ligands that may regulate these processes (Figure 5A). One of the most interesting ligands due to its role in immune suppression in the context of tumorigenesis is IL-6 (Park et al., 2017). In fact, the *IL6* gene is significantly overexpressed in TolDCs compared with DCs (Figure 5B), and its target genes were also observed to be overexpressed in TolDCs (Figure 5C).

We then performed gene set enrichment analysis (GSEA) of differentially expressed genes between DCs and TolDCs and visualized that genes differentially overexpressed in TolDCs were enriched in IL-6-JAK-STAT3 signaling pathway (Figure 5D).

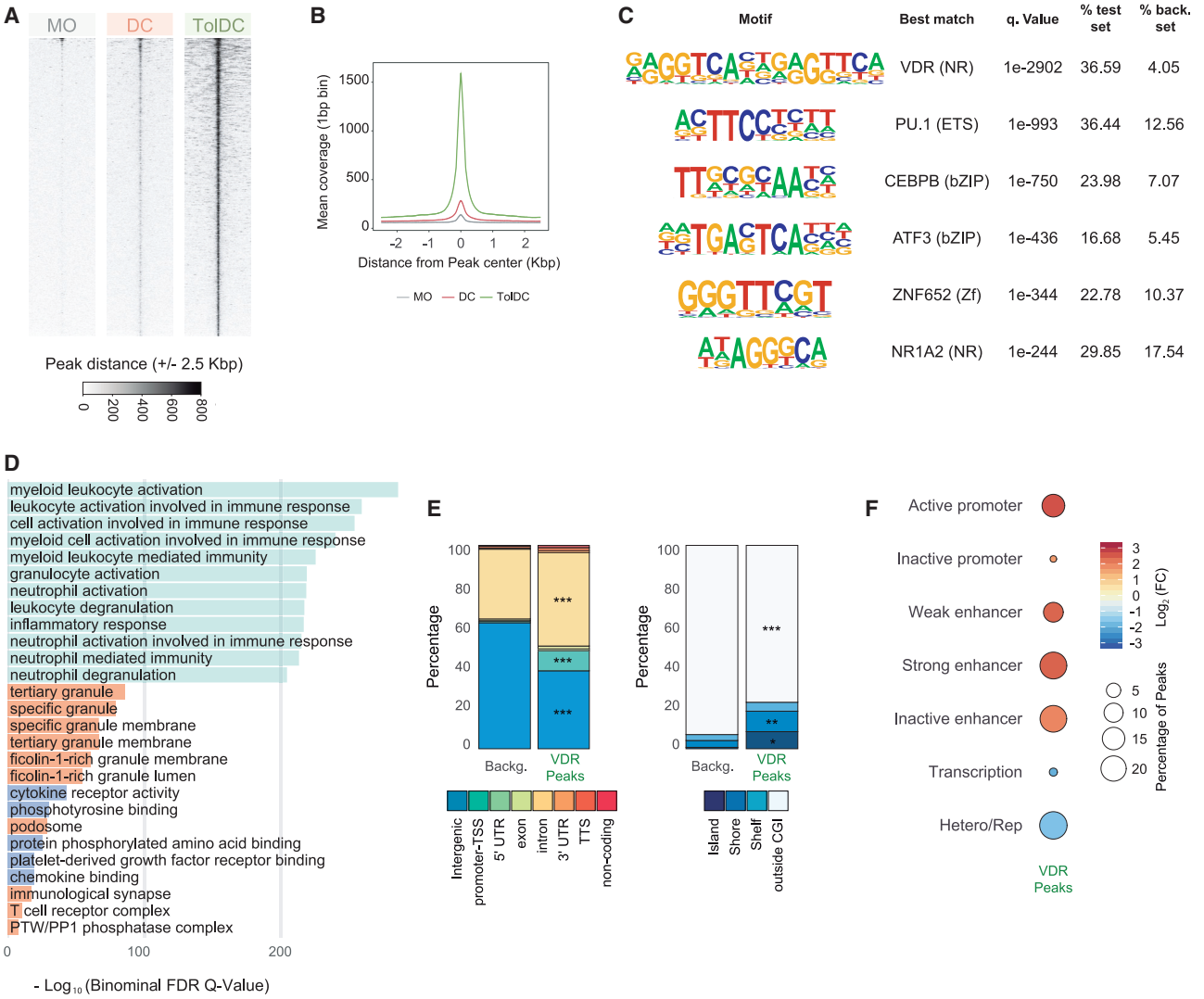

Figure 3. Genomic occupancy of vitamin D receptor (ChIP-seq, n = 2, one experiment)

(A) Heatmaps showing signal intensity of vitamin D receptor (VDR) ChIP-seq at ± 2.5 Kbp window of significant VDR peaks in MO, DCs and TolDCs (q value < 0.01 and irreproducible discovery rate [IDR] < 0.05).

(B) Composite plots of VDR ChIP-seq distribution ±2.5 Kbp around CpGs in MO (gray), DCs (red), and TolDCs (green) for significant VDR peaks. The statistics were computed by comparing the intensity averages of the entire window.

(C) Motif discovery analysis using HOMER software showing q values and the percentage of test and background regions with each motif.

(D) Results of gene set enrichment analysis using GREAT software. The plot depicts the top enriched terms for biological processes (green), molecular function (orange), and cellular component (purple) categories, based on adjusted p values from the binomial distribution.

(E) Location proportions of VDR peaks in the context of CpG islands (CGIs) (right) and gene-related regions (left).

(F) Bubble chart depicting the enrichment (red) or depletion (blue) of VDR peaks in the chromatin states of dendritic cells (Pacis et al., 2015). The circle filling represents the logarithm of the ratio between the percentage of VDR peaks with the feature and the percentage of the feature within the background. Circle size indicates the percentage of VDR peaks in the chromatin state, and the circle edge indicates the statistical significance of the enrichment (black: significant; no edge: not significant; q value < 0.01).

Statistical tests: two-tailed t test (A and B), cumulative binomial distribution (C and D), and two-tailed Fisher's exact test (E and F) (*p < 0.05; **p < 0.01; ***p < 0.001; ****p < 0.0001).

In fact, VDR binds in several regions upstream of the *IL6* gene TSS, suggesting that VDR directly regulates its expression (Figure 5E). Furthermore, we detected an increase in IL-6 production and release into the medium in TolDCs (Figure S4A), which was concordant with an upregulation of its gene expression compared with DCs (Figure 5B). Additionally, significant DNA demethylation was observed in 2 CpG sites of the promoter region of *IL6* in TolDCs, and this was coupled with a gain in 5hmC (Figures S4B and S4C), which suggested the involvement of TET2 in its regulation.

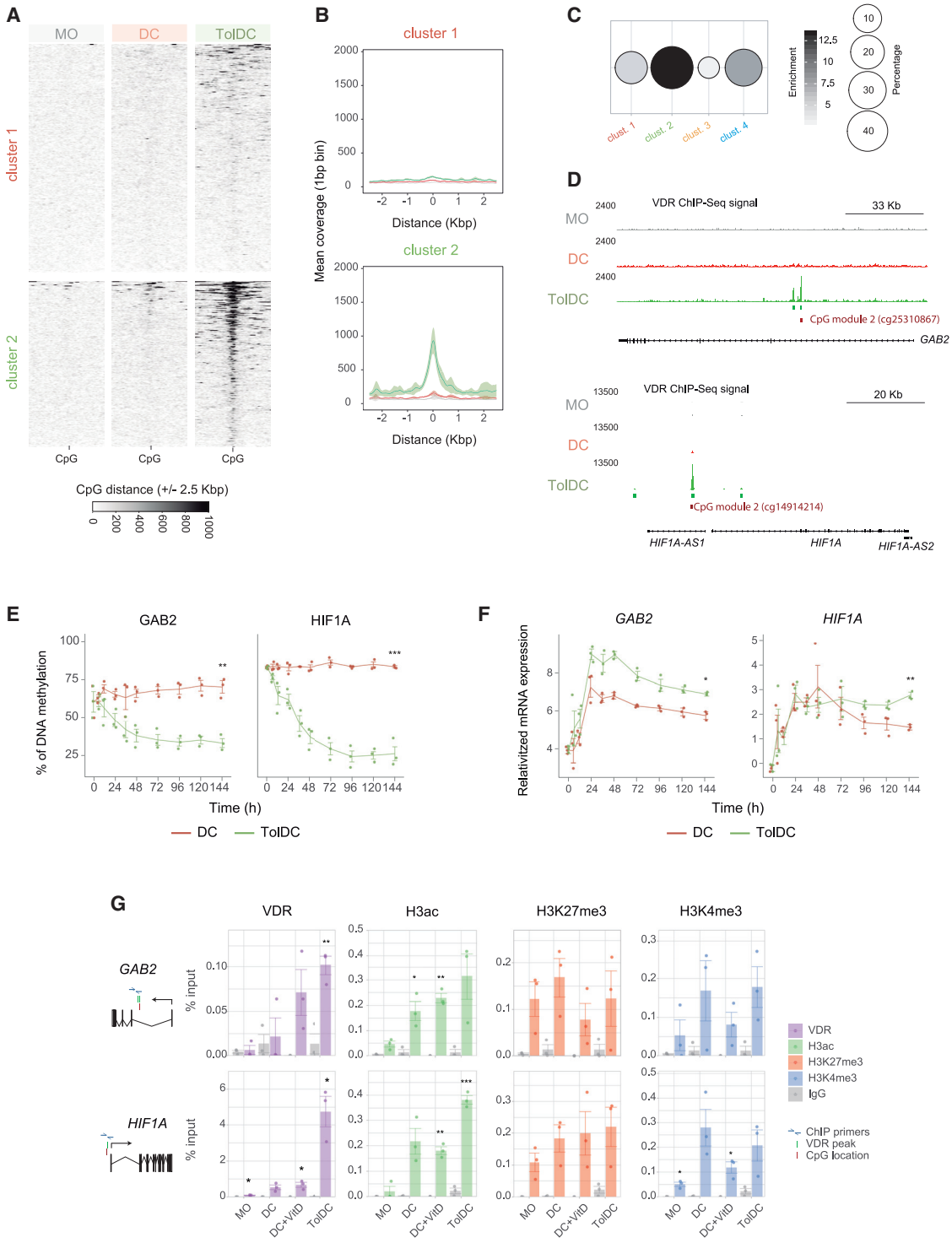

Figure 4. Binding of vitamin D receptor correlates with TolDC-specific DNA demethylation (ChIP-seq, n = 2, one single experiment; DNA methylation, n = 4, two independent experiments)

(A) Heatmaps showing signal intensity of vitamin D receptor (VDR) ChIP-seq at ± 2.5 Kbp window from CpGs of cluster 1 (top) and cluster 2 (bottom) in MO, DCs, and TolDCs.

(B) Composite plots of VDR ChIP-seq distribution ±2.5 Kbp around CpGs from cluster 1 (top) and cluster 2 (bottom) in MO (gray), DC (red), and TolDC (green). Smooth represents the CIs.

(legend continued on next page)

Remarkably, when we blocked IL-6 with an anti-IL-6 antibody during TolDC differentiation, we observed the production of decreased levels of IL-10 (Figure S4D), which is involved in tolerogenesis (Morante-Palacios et al., 2021). This result is consistent with recent findings in T helper type 1 (Th1) cells (Chauss et al., 2022). However, blocking IL-6 during TolDC differentiation did not result in a reduced ability of TolDCs to suppress $CD8^+$ T cell proliferation (Figure S4E). In contrast, in proliferation assays performed with TolDCs in the presence of anti-IL-6 antibody, we found slightly reduced suppression (Figure S4E). These results suggest that IL-6 is a contributor to the ability to suppress $CD8^+$ T cell proliferation by TolDCs but not critical to the acquisition of such properties during TolDC differentiation.

In parallel, we utilized DoRothEA (discriminant regulon expression analysis), a manually curated human regulon for estimating single-sample TF activities through the expression of their target genes (Garcia-Alonso et al., 2019) to analyze TF activities of several STATs in genes differentially expressed in TolDCs compared with DCs, and observed a specific increase in STAT3 activity that was not observed for other members of the STAT family, at 5 days of differentiation (Figure 5F). Furthermore, we observed a marked increase in phosphorylation of STAT3 in TolDCs compared with DCs, which was not observed for STAT5 (Figures 5G and S4E). Although a statistically significant increase in phosphorylation was observed for STAT1, this increase was not to the same extent as STAT3 and may be due to indirect activation, as previously described (Haan et al., 2005) (Figures 5G and S4F). Thus, our results suggested that vitamin D played a role in STAT3 activation.

To explore the possibility that the observed interplay between VDR and STAT3 involves a physical interaction, we performed co-immunoprecipitation experiments in TolDCs. Our analysis revealed a specific interaction between VDR and phosphorylated (p)-STAT3 in TolDCs (Figure 5H). We also observed that both VDR and p-STAT3 interacted with TET2 (Figure 5I), which suggests that these two TFs play a role in the targeting of TET2-mediated demethylation to their cognate sites.

Inhibition of JAK2-mediated STAT3 activation affects the acquisition of vitamin D-dependent tolerogenesis

We investigated the consequences of inhibiting the JAK2-STAT3 pathway by using TG101348, a pharmacological inhibitor of JAK2 (Lasho et al., 2008), during DC and vitamin D-dependent TolDC differentiation. Following TG101348 treatment, we confirmed the inhibition of STAT3 phosphorylation by western blot (Figure 6A). Given that TG101348 is an inhibitor of JAK2, and therefore can affect upstream signaling of STAT1, STAT3, and STAT5, we checked their phosphorylation and observed that the partial inhibition of p-STAT5 and p-STAT1 did not reach statistical significance in TolDCs, unlike p-STAT3 (Figures S5A and S5B). TG101348 treatment also resulted in a sharp decrease in the production of IL-10 (Figure 6B), an archetypical anti-inflammatory cytokine that is also a *bona fide* target for STAT3 (Schaefer et al., 2009; Ziegler-Heitbrock et al., 2003). In fact, IL-10 secretion by TolDCs is a contributor to the suppression of $CD8^+$ T cell proliferation that is halted when adding anti-IL-10 to proliferation assays (Figure S4E). We also tested the effects of JAK2 inhibition on surface markers and observed that JAK2 inhibition resulted in an increase of CD14 and CD86 protein levels and downregulation of CD1a and CD11b (Figure 6C). In parallel, we investigated the effects of JAK2 inhibition on the DNA methylation and expression levels of TolDC-specific demethylated genes. We did not observe any clear reversion of DNA demethylation (Figure 6D), but we did note alterations at the transcriptional level (Figure 6E). Changes were observed not only in cluster 2 genes (TolDC-specific), such as *CD14* and *DPF3*, but also in those of cluster 1, such as *IRF4* and *RASF5* (Figure 6E). These are likely to be the result of the partial inhibition of phosphorylation of STAT1 and STAT5, which might also be involved in activating these and other DC and TolDC genes.

Most importantly, JAK2 inhibition by TG101348 treatment during differentiation resulted in the loss of the ability to suppress $CD8^+$ T cell proliferation of DC differentiated in the presence of vitamin D. This reinforces the idea that the activities of VDR and the JAK2-STAT3 pathway coordinate the acquisition of tolerogenic properties of DCs in the presence of vitamin D (Figure 6F).

DISCUSSION

In this study, we demonstrate that vitamin D is able to induce tolerogenesis in DCs through a mechanism that involves VDR-specific demethylation and activation of key immune genes in a manner that is coordinated with JAK2-mediated STAT3 activation. VDR not only is able to orchestrate a direct response on key immune targets but also associates with activation of the IL-6-JAK-STAT signaling pathway. We also prove the recruitment of TET2 and p-STAT3 by VDR, associated with the

(C) Bubble plot representation of significant VDR binding enrichment in each cluster of CpGs. Dots are colored according to their enrichment value, defined as the logarithm of the ratio between the percentage of CpGs with VDR peak within the cluster and the percentage of CpGs with the VDR peak within the background. Bubble size corresponds to the percentage of CpGs in each cluster overlapping with significant VDR peaks. The presence of a black border indicates significant enrichment (q value < 0.01).
(D) VDR ChIP-seq signal profiles in the vicinity of the representative genes of CpGs from cluster 2. VDR signals are colored by cell type. At the bottom, the significant VDR binding sites are shown in green and CpG position in red.
(E) DNA methylation kinetics of two representative CpGs annotated to GAB2 (cg25310867) and HIF1A (cg14914214) in DCs and TolDCs (n = 3, one experiment).
(F) Gene expression kinetics of GAB2 and HIF1a in DCs and TolDCs (n = 3, one experiment).
(G) Bar plot representation of ChIP-qPCR results for VDR binding and three histone modifications (H3ac, H3K27me3, and H3K4me4) in the vicinity of VDR peaks close to GAB2 and HIF1A gene sequences (n = 3, one experiment). This analysis was performed in MOs, DCs, and TolDCs and DC + vitD. DC + vitD involves adding vitamin D for 30 min at the end of a 6-day differentiation to DCs. Immunoprecipitation with IgG was used as control. The location of the ChIP primers, the CpG site and the VDR peaks are indicated.
Statistical tests: two-tailed Fisher's exact test (C) and unpaired two-tailed t test (E, F, and G) (*p < 0.05; **p < 0.01; ***p < 0.001).

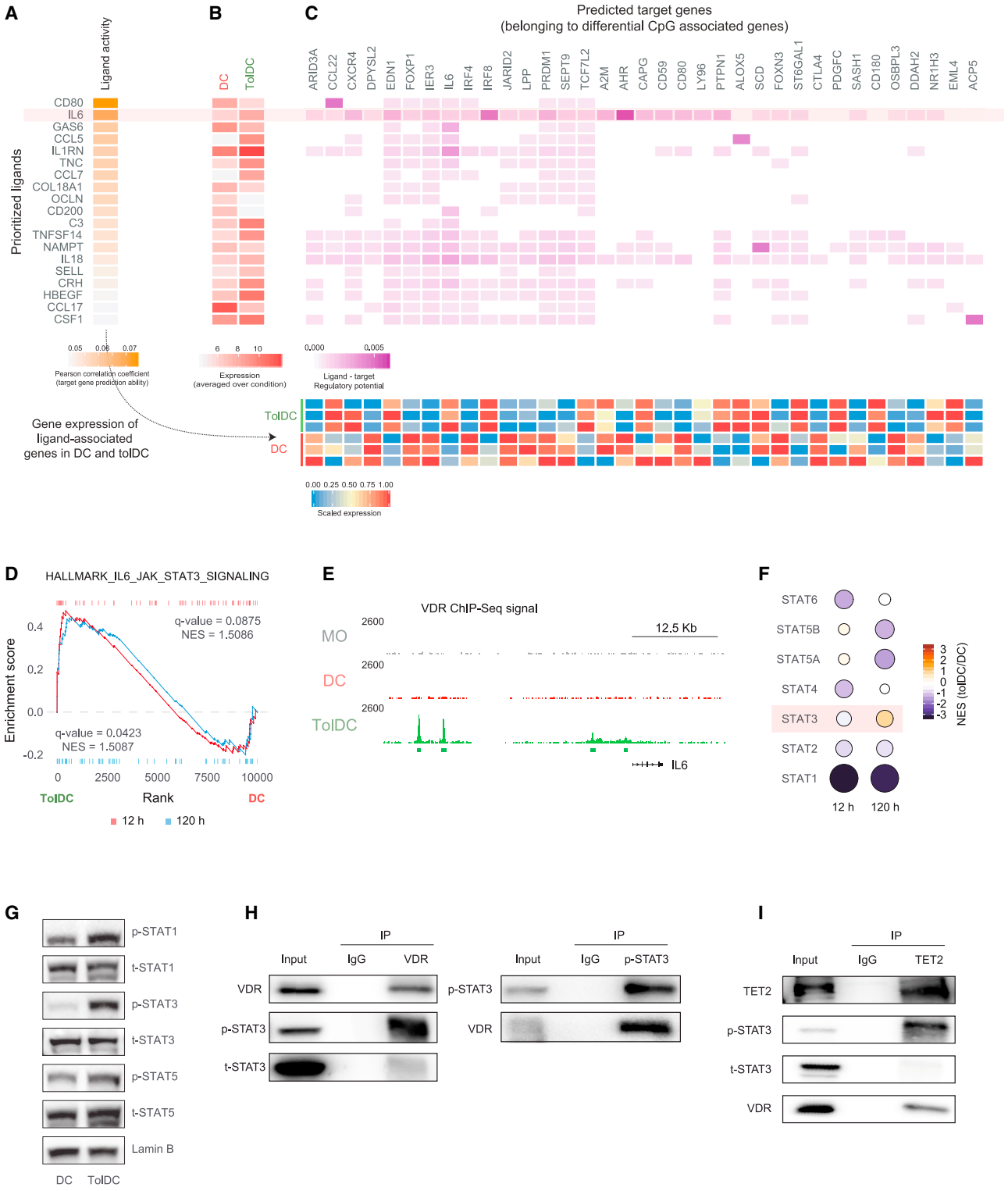

Figure 5. Vitamin D-dependent autocrine/paracrine activation of the IL-6-JAK2-STAT3 pathway

(A) Heatmap showing ligand activity prediction based on the Pearson correlation with its target genes.

(B) Heatmap displaying average gene expression of ligands for DCs and TolDCs on day 5.

(C) Heatmap showing the regulatory potential of each ligand on the target genes based on nichenetr package database (upper panel) and the expression levels of these target genes in each sample (lower panel).

(legend continued on next page)

demethylation and activation of target genes. The essential role of the JAK2-STAT3 pathway in the acquisition of tolerogenesis is demonstrated by the functional impact of the pharmacological inhibition of this pathway.

Our results show the direct role of VDR in guiding TET-mediated DNA demethylation to specific genomic sites during TolDC differentiation. We have shown that, in the presence of vitamin D, VDR levels are increased in the nucleus and that interaction with p-STAT3 and TET2 occurs, thereby promoting TolDC-specific demethylation. A recurrent question in the DNA methylation field is whether DNA methylation is causally involved in shaping gene expression profiles or if it passively reflects transcriptional states (Schübeler, 2015). Our own data support both possibilities, and some DNA methylation changes appear to be more likely to occur after a change in expression than others (Pacis et al., 2019). In our study, we present evidence that TET-mediated demethylation acts as a mechanism facilitating subsequent participation of other TFs, in this case STAT3. In fact, the absence of interference with DNA demethylation, while activation is impeded following pharmacological inhibition of STAT3 phosphorylation, suggests that VDR-dependent demethylation is necessary and precedes STAT3-mediated gene activation. This proposed mechanism was consistent with the alterations in TF activity reported in TET2 knockout mice (Rasmussen et al., 2019). TET2-associated functions may ensure the binding of some TFs, thereby contributing to enhancer-dependent activity and gene expression.

Our study identifies a crucial role for the JAK2-STAT3 pathway in the acquisition of tolerogenesis in innate immunity. The involvement of STAT3 is also relevant in the context of MDSCs, which are also characterized by their tolerogenic properties (Corzo et al., 2009; Kumar et al., 2016). We show that the pharmacological impairment of STAT3 phosphorylation, by inhibiting JAK2, directly results in the loss of the tolerogenic properties of TolDCs, which facilitate T-cell proliferation, demonstrating the essential role of this pathway for the tolerogenic phenotype. Our results raise the possibility that tolerogenic properties can be reverted, not only in the context of vitamin D but also in others. These findings could be clinically relevant both in the context of pathological situations where tolerogenic properties are not desired, like in the tumor microenvironment or in metastatic processes (reviewed in DeVito et al., 2019), as well as in those where they are intentionally pursued (reviewed in Cauwels and Tavernier, 2020), including their therapeutic use in the treatment of inflammatory conditions, such as rheumatoid arthritis and multiple sclerosis (Morante-Palacios et al., 2021).

Limitations of the study

One of the limitations of our current study is that we have not fully explored the impact of the VDR and the IL-6-JAK-STAT3 pathway *in vivo*, in patients treated or supplemented with vitamin D. It would have also been relevant to analyze the direct impact of STAT3 in the epigenetic remodeling in TolDCs, by analyzing their binding sites and associated expression changes. This partly limits our conclusions on the extent and relevance of STAT3 in determining the acquisition of the tolerogenic phenotype.

STAR★METHODS

Detailed methods are provided in the online version of this paper and include the following:

- KEY RESOURCES TABLE
- RESOURCE AVAILABILITY
  - Lead contact
  - Materials availability
  - Data and code availability
- EXPERIMENTAL MODEL AND SUBJECT DETAILS
  - Differentiation of TolDCs and DCs from peripheral blood monocytes
  - Isolation and culture of peripheral blood DCs
- METHOD DETAILS
  - $CD8^+$ cell proliferation assay
  - BrdU proliferation assay
  - Flow cytometry
  - Cytokine measurements
  - Genomic DNA and total RNA extraction
  - Bisulfite (BS) and oxidative-bisulfite (oxBS) pyrosequencing
  - Real-time quantitative Polymerase Chain Reaction (RT-qPCR)
  - Western blot
  - Co-immunoprecipitation (Co-IP)
  - DNA methylation profiling
  - ChIP-seq analysis
  - ChIP-qPCR
  - Microarray reanalysis
  - Data analysis
- QUANTIFICATION AND STATISTICAL ANALYSIS

SUPPLEMENTAL INFORMATION

Supplemental information can be found online at https://doi.org/10.1016/j.celrep.2021.110244.

(D) Gene set enrichment analysis of differentially expressed genes (fold-change < 0.5 or >2 and q-value < 0.05) at 12 h (red) and 120 h (blue). Results for the IL-6-JAK-STAT signaling pathway are shown.
(E) VDR ChIP-seq signal profiles in the vicinity of the *IL6* gene. VDR signals are colored by cell type. The significant VDR binding sites are shown below in green.
(F) Bubble chart depicting the TF activity predicted from mRNA expression of target genes with DoRothEA v2.0. The circle filling represents the normalized enrichment score (NES) (blue: more activity in DCs; red: more activity in TolDCs). Bubble size corresponds to the logarithm of adjusted p values.
(G) Representative western blot assays showing the phosphorylated and total protein levels of STAT1, STAT3, and STAT5 on day 3 of differentiation of DCs and TolDCs (n = 4, two independent experiments).
(H) Representative western blots showing the results of co-immunoprecipitation assays performed in MOs differentiated to DC and TolDC for 3 days. Protein extracts were immunoprecipitated using anti-VDR or anti-p-STAT3 antibodies (n = 3, two independent experiments).
(I) Representative western blots showing the results of co-immunoprecipitation assays performed in MOs differentiated to TolDC for 3 days (n = 3, two independent experiments). Protein extracts were immunoprecipitated using anti-TET2 antibodies.
In both (H and I), IgG was used as a negative control and total protein extract was used as input.

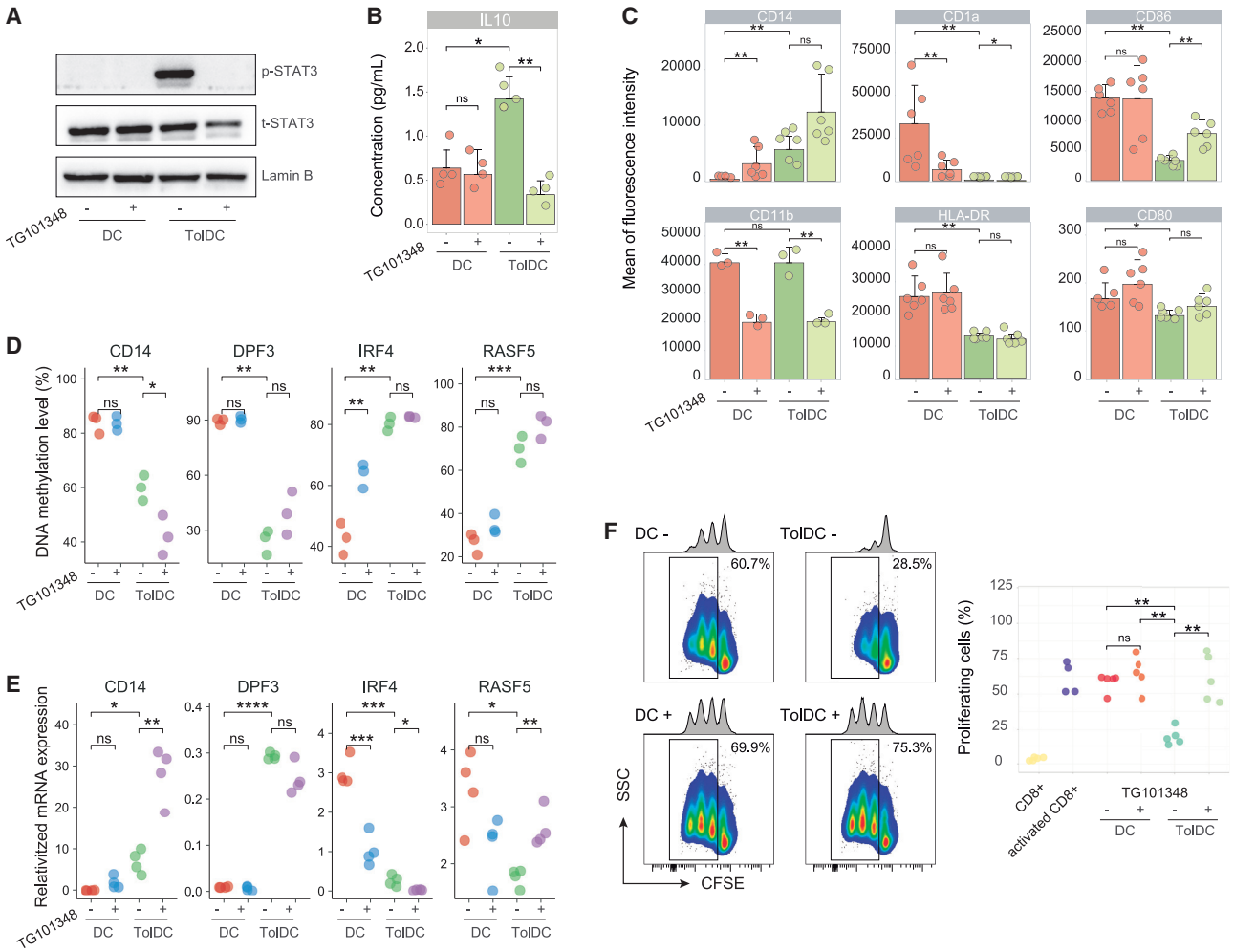

Figure 6. Inhibition of STAT3 phosphorylation reverts immunosuppressive properties of vitamin D exposed dendritic cells

(A) Representative western blot assays showing the effects of STAT3 at the protein phosphorylation level after pharmacological inhibition of JAK2 with TG101348 (n = 3, two experiments).

(B) Bar plot representation of the effect of JAK2 inhibition with TG101348 on IL-10 released by DCs and TolDCs (n = 4, two independent experiments). Protein levels were measured by ELISA.

(C) Bar plots showing the impact of JAK2 inhibition with TG101348 on membrane receptor expression (n = 6, two independent experiments). Protein levels were measured with flow cytometry.

(D) Dot plot representation of bisulfite pyrosequencing results of four example CpGs, two from cluster 1 (CD14 and DPF3) and two from cluster 2 (C1QB and RASF5), displaying the consequence of JAK2 inhibition with TG101348 in DCs and TolDCs (n = 3, two independent experiments).

(E) Dot plot showing mRNA expression of four example genes from cluster 1 and cluster 2 as measured by RT-qPCR, showing the effect of JAK2 inhibition with TG101348 in DCs and TolDCs (n = 4, two independent experiments). Expression was relativized with respect to RPL38 gene expression.

(F) Representative example and dot plot showing the effect on $CD8^+$ cell proliferation of DCs and TolDC generated from MO in presence or absence of TG101348 (n = 5, two independent experiments).

Statistical tests: two-tailed Wilcoxon rank-sum test (B–F) (*p < 0.05; **p < 0.01; ***p < 0.001; ****p < 0.0001).

ACKNOWLEDGMENTS

We are very grateful to Dr. José Luis Sardina for useful feedback. We thank CERCA Programme/Generalitat de Catalunya and the Josep Carreras Foundation for institutional support. E.B. was funded by the Spanish Ministry of Science and Innovation (MICINN; grant number PID2020-117212RB-I00/AEI/10.13039/501100011033). E.M.-C. is funded with RESTORE project (EU H2020 Research and Innovation Programme, number 779316) and Spanish projects PI17/01521 and PI20/01313, integrated in the Plan Nacional de I+D+I and co-supported by the ISCIII-Subdirección General de Evaluación and FEDER. O.M.-P. holds an i-PFIS PhD fellowship (grant number IFI17/00034) from Acción Estratégica en Salud 2013–2016 ISCIII, co-financed by Fondo Social Europeo. F.F. holds a PhD fellowship from the INsTRuCT Consortium, which receives. Innovative Training Network subsidy from the EU H2020 program.

AUTHOR CONTRIBUTIONS

F.C.-M. and E.B. conceived and designed the study; F.C.-M., A.G.F.-B., G.G.-T., O.M.-P., L.C., L.B., F.F., and T.L. performed the differentiation,

chromatin immunoprecipitation, co-immunoprecipitation experiments, and immunological assays; F.C.-M. performed the bioinformatic analyses; F.C.-M., A.G.F.-B., G.G.-T., E.M.-C., and E.B. analyzed results; J.R.-U. and E.B. supervised the study; F.C.-M., T.L., and E.B. wrote the manuscript; all authors participated in discussions and interpreting the results.

DECLARATION OF INTERESTS

The authors declare no competing interests.

Received: June 29, 2021
Revised: September 27, 2021
Accepted: December 20, 2021
Published: January 18, 2022

REFERENCES

Álvarez-Errico, D., Vento-Tormo, R., Sieweke, M., and Ballestar, E. (2015). Epigenetic control of myeloid cell differentiation, identity and function. Nat. Rev. Immunol. *15*, 7–17.

Aryee, M.J., Jaffe, A.E., Corrada-Bravo, H., Ladd-Acosta, C., Feinberg, A.P., Hansen, K.D., and Irizarry, R.A. (2014). Minfi: a flexible and comprehensive bioconductor package for the analysis of infinium DNA methylation microarrays. Bioinformatics *30*, 1363–1369.

Assenov, Y., Müller, F., Lutsik, P., Walter, J., Lengauer, T., and Bock, C. (2014). Comprehensive analysis of DNA methylation data with RnBeads. Nat. Methods *11*, 1138–1140.

Barragan, M., Good, M., and Kolls, J.K. (2015). Regulation of dendritic cell function by vitamin D. Nutrients *7*, 8127–8151.

Bibikova, M., Lin, Z., Zhou, L., Chudin, E., Garcia, E.W., Wu, B., Doucet, D., Thomas, N.J., Wang, Y., Vollmer, E., et al. (2006). High-throughput DNA methylation profiling using universal bead arrays. Genome Res. *16*, 383–393.

Browaeys, R., Saelens, W., and Saeys, Y. (2020). NicheNet: modeling intercellular communication by linking ligands to target genes. Nat. Methods *17*, 159–162.

Bscheider, M., and Butcher, E.C. (2016). Vitamin D immunoregulation through dendritic cells. Immunology *148*, 227–236.

Carlberg, C. (2019). Vitamin D signaling in the context of innate immunity: focus on human monocytes. Front. Immunol. *10*, 2211.

Carvalho, B.S., and Irizarry, R.A. (2010). A framework for oligonucleotide microarray preprocessing. Bioinformatics *26*, 2363–2367.

Cauwels, A., and Tavernier, J. (2020). Tolerizing strategies for the treatment of autoimmune diseases: from ex vivo to in vivo strategies. Front. Immunol. *11*, 674.

Chauss, D., Freiwald, T., McGregor, R., Yan, B., Wang, L., Nova-Lamperti, E., Kumar, D., Zhang, Z., Teague, H., West, E.E., et al. (2022). Autocrine vitamin D signaling switches off pro-inflammatory programs of T H 1 cells. Nat. Immunol. *23*, 62–74.

Chu, C.C., Ali, N., Karagiannis, P., Di Meglio, P., Skowera, A., Napolitano, L., Barinaga, G., Grys, K., Sharif-Paghaleh, E., Karagiannis, S.N., et al. (2012). Resident CD141 (BDCA3) + dendritic cells in human skin produce IL-10 and induce regulatory T cells that suppress skin inflammation. J. Exp. Med. *209*, 935–945.

Corzo, C.A., Cotter, M.J., Cheng, P., Cheng, F., Kusmartsev, S., Sotomayor, E., Padhya, T., McCaffrey, T.V., McCaffrey, J.C., and Gabrilovich, D.I. (2009). Mechanism regulating reactive oxygen species in tumor-induced myeloid-derived suppressor cells. J. Immunol. *182*, 5693–5701.

Corzo, C.A., Condamine, T., Lu, L., Cotter, M.J., Youn, J.I., Cheng, P., Cho, H.I., Celis, E., Quiceno, D.G., Padhya, T., et al. (2010). HIF-1α regulates function and differentiation of myeloid-derived suppressor cells in the tumor microenvironment. J. Exp. Med. *207*, 2439–2453.

Costa, Y., Ding, J., Theunissen, T.W., Faiola, F., Hore, T.A., Shliaha, P.V., Fidalgo, M., Saunders, A., Lawrence, M., Dietmann, S., et al. (2013). NANOG-dependent function of TET1 and TET2 in establishment of pluripotency. Nature *495*, 370–374.

Dankers, W., Colin, E.M., van Hamburg, J.P., and Lubberts, E. (2017). Vitamin D in autoimmunity: molecular mechanisms and therapeutic potential. Front. Immunol. *7*, 697.

de la Rica, L., Rodríguez-Ubreva, J., García, M., Islam, A.B.M.M.K., Urquiza, J.M., Hernando, H., Christensen, J., Helin, K., Gómez-Vaquero, C., and Ballestar, E. (2013). PU.1 target genes undergo Tet2-coupled demethylation and DNMT3b-mediated methylation in monocyte-to-osteoclast differentiation. Genome Biol. *14*, R99.

Deplus, R., Delatte, B., Schwinn, M.K., Defrance, M., Méndez, J., Murphy, N., Dawson, M.A., Volkmar, M., Putmans, P., Calonne, E., et al. (2013). TET2 and TET3 regulate GlcNAcylation and H3K4 methylation through OGT and SET1/COMPASS. EMBO J. *32*, 645–655.

DeVito, N.C., Plebanek, M.P., Theivanthiran, B., and Hanks, B.A. (2019). Role of tumor-mediated dendritic cell Tolerization in immune evasion. Front. Immunol. *10*, 2876.

Feingold, E.A., Good, P.J., Guyer, M.S., Kamholz, S., Liefer, L., Wetterstrand, K., Collins, F.S., Gingeras, T.R., Kampa, D., Sekinger, E.A., et al. (2004). The ENCODE (ENCyclopedia of DNA elements) project. Science *306*, 636–640.

Ferreira, G.B., Overbergh, L., Verstuyf, A., and Mathieu, C. (2013). 1α,25-Dihydroxyvitamin D3 and its analogs as modulators of human dendritic cells: a comparison dose-titration study. J. Steroid Biochem. Mol. Biol. *136*, 160–165.

Ferreira, G.B., Vanherwegen, A.S., Eelen, G., Gutiérrez, A.C.F., VanLommel, L., Marchal, K., Verlinden, L., Verstuyf, A., Nogueira, T., Georgiadou, M., et al. (2015). Vitamin D3 induces tolerance in human dendritic cells by activation of intracellular metabolic pathways. Cell Rep. *10*, 711–725.

Fetahu, I.S., Höbaus, J., and Kállay, E. (2014). Vitamin D and the epigenome. Front. Physiol. *5*, 164.

Garcia-Alonso, L., Holland, C.H., Ibrahim, M.M., Turei, D., and Saez-Rodriguez, J. (2019). Benchmark and integration of resources for the estimation of human transcription factor activities. Genome Res. *29*, 1363–1375.

Garcia-Gomez, A., Li, T., Kerick, M., Català-Moll, F., Comet, N.R., Rodríguez-Ubreva, J., De La Rica, L., Branco, M.R., Martín, J., and Ballestar, E. (2017). TET2- and TDG-mediated changes are required for the acquisition of distinct histone modifications in divergent terminal differentiation of myeloid cells. Nucleic Acids Res. *45*, 10002–10017.

Goudot, C., Coillard, A., Villani, A.C., Gueguen, P., Cros, A., Sarkizova, S., Tang-Huau, T.L., Bohec, M., Baulande, S., Hacohen, N., et al. (2017). Aryl hydrocarbon receptor controls monocyte differentiation into dendritic cells versus macrophages. Immunity *47*, 582–596.e6.

Guilhamon, P., Eskandarpour, M., Halai, D., Wilson, G.A., Feber, A., Teschendorff, A.E., Gomez, V., Hergovich, A., Tirabosco, R., Fernanda Amary, M., et al. (2013). Meta-analysis of IDH-mutant cancers identifies EBF1 as an interaction partner for TET2. Nat. Commun. *4*, 2166.

Haan, S., Keller, J.F., Behrmann, I., Heinrich, P.C., and Haan, C. (2005). Multiple reasons for an inefficient STAT1 response upon IL-6-type cytokine stimulation. Cell. Signal. *17*, 1542–1550.

Heinz, S., Benner, C., Spann, N., Bertolino, E., Lin, Y.C., Laslo, P., Cheng, J.X., Murre, C., Singh, H., and Glass, C.K. (2010). Simple combinations of lineage-determining transcription factors prime cis-regulatory elements required for macrophage and B cell identities. Mol. Cell *38*, 576–589.

Ichiyama, K., Chen, T., Wang, X., Yan, X., Kim, B.S., Tanaka, S., Ndiaye-Lobry, D., Deng, Y., Zou, Y., Zheng, P., et al. (2015). The methylcytosine dioxygenase Tet2 promotes DNA demethylation and activation of cytokine gene expression in T cells. Immunity *42*, 613–626.

Jakob, F., Gieseler, F., Tresch, A., Hammer, S., Seufert, J., and Schneider, D. (1992). Kinetics of nuclear translocation and turnover of the vitamin D receptor in human HL60 leukemia cells and peripheral blood lymphocytes-coincident rise of DNA-relaxing activity in nuclear extracts. J. Steroid Biochem. Mol. Biol. *42*, 11–16.

Jones, P.A. (2012). Functions of DNA methylation: islands, start sites, gene bodies and beyond. Nat. Rev. Genet. *13*, 484–492.

Klug, M., Schmidhofer, S., Gebhard, C., Andreesen, R., and Rehli, M. (2013). 5-Hydroxymethylcytosine is an essential intermediate of active DNA demethylation processes in primary human monocytes. Genome Biol. *14*, R46.

Koressaar, T., and Remm, M. (2007). Enhancements and modifications of primer design program primer3. Bioinformatics *23*, 1289–1291.

Korotkevich, G., Sukhov, V., and Sergushichev, A. (2019). Fast gene set enrichment analysis. BioRxiv. https://doi.org/10.1101/060012.

Kumar, V., Cheng, P., Condamine, T., Mony, S., Languino, L.R., McCaffrey, J.C., Hockstein, N., Guarino, M., Masters, G., Penman, E., et al. (2016). CD45 phosphatase inhibits STAT3 transcription factor activity in myeloid cells and promotes tumor-associated macrophage differentiation. Immunity *44*, 303–315.

Langmead, B., and Salzberg, S.L. (2012). Fast gapped-read alignment with Bowtie 2. Nat. Methods *9*, 357–359.

Lasho, T.L., Tefferi, A., Hood, J.D., Verstovsek, S., Gilliland, D.G., and Pardanani, A. (2008). TG101348, a JAK2-selective antagonist, inhibits primary hematopoietic cells derived from myeloproliferative disorder patients with JAK2V617F, MPLW515K or JAK2 exon 12 mutations as well as mutation negative patients. Leukemia *22*, 1790–1792.

Leek, J.T., Johnson, W.E., Parker, H.S., Fertig, E.J., Jaffe, A.E., Zhang, Y., Storey, J.D., Torres, L.C., 2021. Bioconductor. sva: Surrogate Variable Analysis. R package version 3.42.0.

Li, H., Handsaker, B., Wysoker, A., Fennell, T., Ruan, J., Homer, N., Marth, G., Abecasis, G., and Durbin, R. (2009). The sequence alignment/map format and SAMtools. Bioinformatics *25*, 2078–2079.

Li, T., Garcia-Gomez, A., Morante-Palacios, O., Ciudad, L., Özkaramehmet, S., Van Dijck, E., Rodríguez-Ubreva, J., Vaquero, A., and Ballestar, E. (2020). SIRT1/2 orchestrate acquisition of DNA methylation and loss of histone H3 activating marks to prevent premature activation of inflammatory genes in macrophages. Nucleic Acids Res. *48*, 665–681.

Lio, C.W., Zhang, J., González-Avalos, E., Hogan, P.G., Chang, X., and Rao, A. (2016). Tet2 and Tet3 cooperate with B-lineage transcription factors to regulate DNA modification and chromatin accessibility. Elife *5*, e18290.

Liu, J., Zhang, X., Chen, K., Cheng, Y., Liu, S., Xia, M., Chen, Y., Zhu, H., Li, Z., and Cao, X. (2019). CCR7 chemokine receptor-inducible lnc-Dpf3 restrains dendritic cell migration by inhibiting HIF-1α-Mediated glycolysis. Immunity *50*, 600–615.e15.

Luo, C., Hajkova, P., and Ecker, J.R. (2018). Dynamic DNA methylation: in the right place at the right time. Science *361*, 1336–1340.

Mahé, E.A., Madigou, T., Sérandour, A.A., Bizot, M., Avner, S., Chalmel, F., Palierne, G., Métivier, R., and Salbert, G. (2017). Cytosine modifications modulate the chromatin architecture of transcriptional enhancers. Genome Res. *27*, 947–958.

McLean, C.Y., Bristor, D., Hiller, M., Clarke, S.L., Schaar, B.T., Lowe, C.B., Wenger, A.M., and Bejerano, G. (2010). GREAT improves functional interpretation of cis-regulatory regions. Nat. Biotechnol. *28*, 495–501.

Mendes, K., Schmidhofer, S., Minderjahn, J., Glatz, D., Kiesewetter, C., Raithel, J., Wimmer, J., Gebhard, C., and Rehli, M. (2021). The epigenetic pioneer EGR2 initiates DNA demethylation in differentiating monocytes at both stable and transient binding sites. Nat. Commun. *12*, 1556.

Monticelli, S., and Natoli, G. (2017). Transcriptional determination and functional specificity of myeloid cells: making sense of diversity. Nat. Rev. Immunol. *17*, 595–607.

Mora, J.R., Iwata, M., and Von Andrian, U.H. (2008). Vitamin effects on the immune system: vitamins A and D take centre stage. Nat. Rev. Immunol. *8*, 685–698.

Morante-Palacios, O., Fondelli, F., Ballestar, E., and Martínez-Cáceres, E.M. (2021). Tolerogenic dendritic cells in autoimmunity and inflammatory diseases. Trends Immunol. *42*, 59–75.

Müller, F., Scherer, M., Assenov, Y., Lutsik, P., Walter, J., Lengauer, T., and Bock, C. (2019). RnBeads 2.0: comprehensive analysis of DNA methylation data. Genome Biol. *20*, 55.

Murphy, T.L., Grajales-Reyes, G.E., Wu, X., Tussiwand, R., Briseño, C.G., Iwata, A., Kretzer, N.M., Durai, V., and Murphy, K.M. (2016). Transcriptional control of dendritic cell development. Annu. Rev. Immunol. *34*, 93–119.

Navarro-Barriuso, J., Mansilla, M.J., and Martínez-Cáceres, E.M. (2018). Searching for the transcriptomic signature of immune tolerance induction-biomarkers of safety and functionality for tolerogenic dendritic cells and regulatory macrophages. Front. Immunol. *9*, 2062.

Ong, L.T.C., Schibeci, S.D., Fewings, N.L., Booth, D.R., and Parnell, G.P. (2021). Age-dependent VDR peak DNA methylation as a mechanism for latitude-dependent multiple sclerosis risk. Epigenetics Chromatin *14*, 9.

Pacis, A., Tailleux, L., Morin, A.M., Lambourne, J., MacIsaac, J.L., Yotova, V., Dumaine, A., Danckært, A., Luca, F., Grenier, J.C., et al. (2015). Bacterial infection remodels the DNA methylation landscape of human dendritic cells. Genome Res. *25*, 1801–1811.

Pacis, A., Mailhot-Léonard, F., Tailleux, L., Randolph, H.E., Yotova, V., Dumaine, A., Grenier, J.-C., and Barreiro, L.B. (2019). Gene activation precedes DNA demethylation in response to infection in human dendritic cells. Proc. Natl. Acad. Sci. U S A *116*, 6938–6943.

Pageaud, Y., Plass, C., and Assenov, Y. (2018). Enrichment analysis with EpiAnnotator. Bioinformatics *32*, 1781–1783.

Park, J.H., Van Wyk, H., McMillan, D.C., Quinn, J., Clark, J., Roxburgh, C.S.D., Horgan, P.G., and Edwards, J. (2017). Signal transduction and activator of transcription-3 (STAT3) in patients with colorectal cancer: associations with the phenotypic features of the tumor and host. Clin. Cancer Res. *23*, 1698–1709.

Penna, G., and Adorini, L. (2000). 1α,25-Dihydroxyvitamin D 3 inhibits differentiation, maturation, activation, and survival of dendritic cells leading to impaired alloreactive T cell activation. J. Immunol. *164*, 2405–2411.

Pereira, F., Barbáchano, A., Silva, J., Bonilla, F., Campbell, M.J., Muñoz, A., and Larriba, M.J. (2011). KDM6B/JMJD3 histone demethylase is induced by vitamin D and modulates its effects in colon cancer cells. Hum. Mol. Genet. *20*, 4655–4665.

Piemonti, L., Monti, P., Sironi, M., Fraticelli, P., Leone, B.E., Dal Cin, E., Allavena, P., and Di Carlo, V. (2000). Vitamin D 3 affects differentiation, maturation, and function of human monocyte-derived dendritic cells. J. Immunol. *164*, 4443–4451.

Pratt, J.C., Igras, V.E., Maeda, H., Baksh, S., Gelfand, E.W., Burakoff, S.J., Neel, B.G., and Gu, H. (2000). Cutting edge: gab2 mediates an inhibitory phosphatidylinositol 3'-kinase pathway in T cell antigen receptor signaling. J. Immunol. *165*, 4158–4163.

Ramírez, F., Dündar, F., Sarah Diehl, S., Björn A Grüning, B.A., and Manke, T. (2014). deepTools: a flexible platform for exploring deep-sequencing data. Nucleic Acids Res. *42*, W187–W191.

Rasmussen, K.D., Berest, I., Keβler, S., Nishimura, K., Simón-Carrasco, L., Vassiliou, G.S., Pedersen, M.T., Christensen, J., Zaugg, J.B., and Helin, K. (2019). TET2 binding to enhancers facilitates transcription factor recruitment in hematopoietic cells. Genome Res. *29*, 564–575.

Ritchie, M.E., Phipson, B., Wu, D., Hu, Y., Law, C.W., Shi, W., and Smyth, G.K. (2015). Limma powers differential expression analyses for RNA-sequencing and microarray studies. Nucleic Acids Res. *43*, e47.

Sardina, J.L., Collombet, S., Tian, T.V., Gómez, A., Di Stefano, B., Berenguer, C., Brumbaugh, J., Stadhouders, R., Segura-Morales, C., Gut, M., et al. (2018). Transcription factors drive Tet2-mediated enhancer demethylation to reprogram cell fate. Cell Stem Cell *23*, 727–741.e9.

Schaefer, A., Unterberger, C., Frankenberger, M., Lohrum, M., Staples, K.J., Werner, T., Stunnenberg, H., and Ziegler-Heitbrock, L. (2009). Mechanism of Interferon-gamma mediated down-regulation of Interleukin-10 gene expression. Mol. Immunol. *46*, 1351–1359.

Schübeler, D. (2015). Function and information content of DNA methylation. Nature *517*, 321–326.

Segura, E., Touzot, M., Bohineust, A., Cappuccio, A., Chiocchia, G., Hosmalin, A., Dalod, M., Soumelis, V., and Amigorena, S. (2013). Human inflammatory dendritic cells induce Th17 cell differentiation. Immunity *38*, 336–348.

Seuter, S., Neme, A., and Carlberg, C. (2017). Epigenomic PU.1-VDR crosstalk modulates vitamin D signaling. Biochim. Biophys. Acta Gene Regul. Mech. *1860*, 405–415.

Seuter, S., Neme, A., and Carlberg, C. (2018). ETS transcription factor family member GABPA contributes to vitamin D receptor target gene regulation. J. Steroid Biochem. Mol. Biol. *177*, 46–52.

Széles, L., Keresztes, G., Töröcsik, D., Balajthy, Z., Krenács, L., Póliska, S., Steinmeyer, A., Zuegel, U., Pruenster, M., Rot, A., et al. (2009). 1,25-Dihydroxyvitamin D 3 is an autonomous regulator of the transcriptional changes leading to a tolerogenic dendritic cell phenotype. J. Immunol. *182*, 2074–2083.

Teh, B.K., Yeo, J.G., Chern, L.M., and Lu, J. (2011). C1q regulation of dendritic cell development from monocytes with distinct cytokine production and T cell stimulation. Mol. Immunol. *48*, 1128–1138.

Torres-Aguilar, H., Aguilar-Ruiz, S.R., González-Pérez, G., Munguía, R., Bajaña, S., Meraz-Ríos, M.A., and Sánchez-Torres, C. (2010). Tolerogenic dendritic cells generated with different immunosuppressive cytokines induce antigen-specific anergy and regulatory properties in memory $CD4^+$ T cells. J. Immunol. *184*, 1765–1775.

van der Maaten, L. (2014). Accelerating t-SNE using Tree-based algorithms. J. Machine Learn. Res. *15*, 3221–3245.

Van Halteren, A.G.S., Van Etten, E., De Jong, E.C., Bouillon, R., Roep, B.O., and Mathieu, C. (2002). Redirection of human autoreactive T-cells upon interaction with dendritic cells modulated by TX527, an analog of 1,25 dihydroxyvitamin D3. Diabetes *51*, 2119–2125.

Wang, Y., Xiao, M., Chen, X., Chen, L., Xu, Y., Lv, L., Wang, P., Yang, H., Ma, S., Lin, H., et al. (2015). WT1 recruits TET2 to regulate its target gene expression and suppress leukemia cell proliferation. Mol. Cell *57*, 662–673.

Wei, Z., Yoshihara, E., He, N., Hah, N., Fan, W., Pinto, A.F.M., Huddy, T., Wang, Y., Ross, B., Estepa, G., et al. (2018). Vitamin D switches BAF complexes to protect β cells. Cell *173*, 1135–1149.e15.

Xiong, J., Zhang, Z., Chen, J., Huang, H., Xu, Y., Ding, X., Zheng, Y., Nishinakamura, R., Xu, G.-L., Wang, H., et al. (2016). Cooperative action between SALL4A and TET proteins in stepwise oxidation of 5-methylcytosine. Mol. Cell *64*, 913–925.

Ziegler-Heitbrock, L., Lötzerich, M., Schaefer, A., Werner, T., Frankenberger, M., and Benkhart, E. (2003). IFN-α induces the human IL-10 gene by recruiting both IFN regulatory factor 1 and Stat3. J. Immunol. *171*, 285–290.

STAR★METHODS

KEY RESOURCES TABLE

REAGENT or RESOURCE	SOURCE	IDENTIFIER
Antibodies		
Fc Block reagent, human antibody	Miltenyi Biotec	Cat# 130-059-901; RRID: AB_2892112
Anti-human CD14, FITC conjugated (clone TÜK4)	Miltenyi Biotec	Cat# 130-080-701;RRID: AB_244303
Anti-human CD80, PE conjugated (clone 2D10)	Miltenyi Biotec	Cat# 130-097-202; RRID: AB_2659259
Anti-human CD86, APC conjugated (clone FM95)	Miltenyi Biotec	Cat# 130-113-569; RRID: AB_2726174
Anti-human CD11b, APC conjugated (clone ICRF44)	BioLegend	Cat# 301310; RRID: AB_314162
Anti-human CD1a, PE conjugated (clone HI149)	BioLegend	Cat# 300106; RRID: AB_314020
Anti-human HLA-DR, Pe-Cyanine7 conjugated (clone LN3)	Thermo Fisher Scientific	Cat# 25-9956-42; RRID: AB_1582284
LIVE/DEAD™ Fixable Violet Dead Cell Stain Kit	Thermo Fisher Scientific	Cat# L34964
Anti-acetyl-Histone H3 Antibody	Millipore	Cat# 06-599; RRID: AB_2115283
Anti-trimethyl-Histone H3 (Lys27) Antibody	Millipore	Cat# 07-449; RRID: AB_310624
Anti-Trimethyl-Histone H3 (Lys4)	Millipore	Cat# 17-614; RRID: AB_11212770
Rat IgG1 kappa Isotype Control (clone eBRG1)	Thermo Fisher Scientific	Cat# 16-4301-85; RRID: AB_470154
IL-10 Monoclonal Antibody (clone JES3-9D7)	Thermo Fisher Scientific	Cat# 16-7108-85; RRID: AB_469229
IL-6 Monoclonal Antibody (clone MQ2-13A5)	Thermo Fisher Scientific	Cat# 16-7069-85; RRID: AB_469219
Vitamin D receptor	Cell Signaling Technology	Cat# 12550; RRID: AB_2637002
Anti-TET2 antibodody	Abcam	Cat# ab124297; RRID: AB_2722695
Anti-Pstat3 [Y705], (clone 4/P-STAT3)	Fluidigm	Cat# 3158005A; RRID: AB_2811100
Anti-STAT3, (clone 79D7)	Cell Signaling Technology	Cat# 4904; RRID: AB_331269
Anti-pSTAT1 [Y701], (clone 58D6)	Cell Signaling Technology	Cat# 9167; RRID: AB_561284
Anti-STAT1, (clone 42H3)	Cell Signaling Technology	Cat# 9175; RRID: AB_2197984
Anti-pSTAT5 [Y694], (clone 47)	Fluidigm	Cat# 3150005A; RRID: AB_2744690
Anti-STAT5 beta, (clone ST5b-10G1)	Thermo Fisher Scientific	Cat# 13-5300; RRID: AB_2533021
Anti-Lamin B1	Abcam	Cat# ab16048; RRID: AB_443298
Anti-alpha-Tubulin, (clone DM1A)	Sigma-Aldrich	Cat# T6199; RRID: AB_477583
Normal Rabbit IgG Antibody	Millipore	Cat# 12-370; RRID: AB_145841
Normal Mouse IgG Antibody	Millipore	Cat# 12-371; RRID: AB_145840
Biological samples		
Buffy Coats	Catalan Blood and Tissue Bank (CBTB)	Cat# BB014
Chemicals, peptides, and recombinant proteins		
Recombinant Human IL-4	Peprotech	Cat# 200-04; GenPept: P05112
Recombinant Human GM-CSF	Peprotech	Ca# 300-03; GenPept: P04141
1α,25-Dihydroxyvitamin D3	Sigma-Aldrich	Cat# D1530; CAS: 32222-06-3
TG101348, JAK/STAT pathway inhibitor	STEMCELL	Cat# 73472; CAS: 936091-26-8
Potassium perruthenate (VII) (KRuO4)	Thermo Fisher Scientific	Cat# 11877; CAS: 10378-50-4
Triton™ X-100	Sigma-Aldrich	Cat# T8787; CAS: 9036-19-5
Benzonase® Nuclease	Sigma-Aldrich	Cat# E1014; CAS: 9025-65-4
DMP (Dimethyl Pimelimidate)	Thermo Fisher Scientific	Cat# 21666; CAS: 58537-94-3
Critical commercial assays		
MACS CD14 Microbeads	Miltenyi Biotec	Cat# 130-050-201
CD1c (BDCA-1)+ Dendritic Cell Isolation Kit	Miltenyi Biotec	Cat# 130-119-475
Dynabeads™ Untouched™ Human CD8 T Cells Kit	Thermo Fisher Scientific	Cat# 11348D
Cell Trace CFSE	Thermo Fisher Scientific	Cat# C34554

(*Continued on next page*)

Continued

REAGENT or RESOURCE	SOURCE	IDENTIFIER
APC BrdU Flow Kit	BD Pharmingen	Cat# 552598
ELISA MAXTM Deluxe Set Human IL-10	BioLegend	Cat# 430604
Access IL-6 reagent kit	Beckman-Coulter	Cat# A16369
Maxwell RSC Cultured Cells DNA Kit	Promega	Cat# AS1620
Maxwell RSC simplyRNA cells Kit	Promega	Cat# AS1390
EZ DNA Methylation-Gold Kit	Zymo Research	Cat# D5005
PyroMark Q48 Advanced CpG Reagents	Qiagen	Cat# 974022
Transcriptor First Strand cDNA Synthesis Kit	Roche	Cat# 04897030001
IMMOLASE DNA polymerase Kit	Bioline	Cat# BIO-21047
LightCycler® 480 SYBR Green I Master	Roche	Cat# 0487352001
Infinium MethylationEPIC BeadChip	Illumina	Cat# 20042130
iDeal ChIP-seq kit for Transcription Factors	Diagenode	Cat# C01010055
Magna ChIP™ Protein A+G Magnetic Beads	Sigma-Aldrich	Cat# 16-663
cOmplete™, EDTA-free Protease Inhibitor Cocktail	Sigma-Aldrich	Cat# 11873580001
PureProteome™ Protein G Magnetic Bead System	Sigma-Aldrich	Cat# LSKMAGG02
Micro Bio-Spin® P-6 SSC columns	Bio-Rad	Cat# 7326200
Deposited data		
DNA methylation profile of *in vitro* generated DC and TolDC	This paper	GSE145483
VDR ChIP-Seq	This paper	GSE145584
Oligonucleotides		
Primers for bisulphite pyrosequencing, RT-qPCR and ChIP-qPCR, see Table S2	This paper	N/A
Software and algorithms		
PyroMark Assay Design 2.0 software	Qiagen	Cat# 9019079
Pyromark Q48 Autoprep software	Qiagen	Cat# 9024325
Minfi (R package)	Aryee et al., 2014	https://www.bioconductor.org/packages/release/bioc/html/minfi.html
RnBeads (R package)	Assenov et al. (2014)	https://bioconductor.org/packages/release/bioc/html/RnBeads.html
Limma (R package)	Ritchie et al. (2015)	https://bioconductor.org/packages/release/bioc/html/limma.html
Bowtie2 Aligner v2.2.6	Langmead and Salzberg, 2012	http://bowtie-bio.sourceforge.net/bowtie2/index.shtml
MarkDuplicates software v1.126	Broad institute	https://broadinstitute.github.io/picard/
Sequence Alignment/Map (SAMtools) v1.2	Li et al. (2009)	https://doi.org/10.1093/bioinformatics/btp352
bamCoverage function (deepTools (v2.0))	Ramírez et al. (2014)	https://deeptools.readthedocs.io/en/2.1.0/content/tools/bamCoverage.html
HOMER Motif Analysis	Heinz et al. (2010)	http://homer.ucsd.edu/homer/motif/
GREAT (version 3.0.0.)	McLean et al. (2010)	http://great.stanford.edu/public/html
EpiAnnotator (R package)	Pageaud et al. (2018)	http://epigenomics.dkfz.de/EpiAnnotator/
fgsea (R package)	Korotkevich et al. (2019)	http://bioconductor.org/packages/release/bioc/html/fgsea.html
tSNE	van der Maaten, 2014	https://github.com/lvdmaaten/bhtsne/
sva (R package)	(Leek et al., 2021)	https://bioconductor.org/packages/release/bioc/html/sva.html
DoRothEA (R package)	Garcia-Alonso et al. (2019)	https://bioconductor.org/packages/release/data/experiment/html/dorothea.html
Nichenetr (R package)	Browaeys et al. (2020)	https://github.com/saeyslab/nichenetr

RESOURCE AVAILABILITY

Lead contact

Further information and requests for resources should be directed to the lead contact, Esteban Ballestar (eballestar@carrerasresearch.org).

Materials availability

This study did not generate new unique reagents.

Data and code availability

- DNA methylation and ChIP-seq data for this publication have been deposited in the NCBI Gene Expression Omnibus and are accessible through GEO Series accession numbers GSE145483 and GSE145584.
- This paper does not report original code.
- Any additional information required to reanalyze the data reported in this paper is available from the lead contact upon request

EXPERIMENTAL MODEL AND SUBJECT DETAILS

Differentiation of TolDCs and DCs from peripheral blood monocytes

For *in vitro* differentiation experiments, we obtained buffy coats from anonymous donors through the Catalan Blood and Tissue Bank (CBTB). The CBTB follows the principles of the World Medical Association (WMA) Declaration of Helsinki. The Committee for Human Subjects of Bellvitge Hospital approved the study (PR275/17). Given the anonymous nature of the volunteers, no information about the gender and age was provided by the CBTB. Before providing the first blood sample, all donors received detailed oral and written information, and signed a consent form at the CBTB. Peripheral blood mononuclear cells (PBMCs) were isolated by Ficoll-Paque gradient centrifugation. MOs were isolated from PBMCs using positive selection with MACS CD14 microbeads (Miltenyi Biotec). Cells were resuspended in RPMI Medium 1640 + GlutaMAXTM-1 (Gibco, Life Technologies) containing 10% fetal bovine serum, 100 units/mL penicillin, and 100 μg/mL streptomycin. For TolDC differentiation, the medium was supplemented with 10 ng/mL human IL-4, 10 ng/mL GM-CSF (PeproTech), and 10 nM of vitamin D3 or calcitriol (Sigma Aldrich). For DCs, the medium did not contain vitamin D. Anti-IL-6 1 μg/mL (Invitrogen) and rat IgG isotype 1 μg/mL (eBioscience) was added during differentiation process when required. In some cases, specified in the text, vitamin D3 was added for 30 min following differentiation to DCs (DC + vitD). In other experiments, differentiation was performed in the presence of a JAK2 inhibitor (TG101348, STEMCELL) at 500 nM.

Isolation and culture of peripheral blood DCs

For the validation of our differentiation model, peripheral blood CD1c + DCs were isolated and cultured for three days with or without 100 nM vitamin D (Sigma Aldrich). These samples were also obtained from anonymous donors through the Catalan Blood and Tissue Bank (CBTB). The CBTB follows the principles of the World Medical Association (WMA) Declaration of Helsinki. The Committee for Human Subjects of Bellvitge Hospital approved the study (PR275/17). Given the anonymous nature of the volunteers, no information about the gender and age was provided by the CBTB. Before providing the first blood sample, all donors received detailed oral and written information, and signed a consent form at the CBTB. For this, PBMCs were isolated by Ficoll-Paque gradient centrifugation followed by a CD1c + DCs purification with CD1c (BDCA-1)+. Dendritic Cell Isolation Kit (Miltenyi Biotec) according to manufacturer instructions. Obtained cells were cultured at a concentration of 10^6 cells/mL in RPMI Medium 1640 + GlutaMAXTM-1 (Gibco, Life Technologies) containing 10% fetal bovine serum and 100 units/mL penicillin with or without vitamin D.

METHOD DETAILS

$CD8^+$ cell proliferation assay

Allogenic $CD8^+$ T-cells isolated using negative selection with the human CD8 T Cells Kit (Invitrogen) were labeled with carboxyfluorescein succinimidyl ester (CFSE) and seeded in 96-well plates at 200,000 cells/well, with TolDCs or DCs at different ratios (TolDC/DC:CD8+ T-cell ratios: 1:2, 1:4, and 1:6). $CD8^+$ cells were then stimulated with anti-CD3/CD28 Dynabeads 5 μL/mL (Invitrogen) and cultured for 5 days. Anti-IL-6 1 μg/mL (Invitrogen), anti-IL-10 1 μg/mL (eBioscience) and rat IgG isotype 1 μg/mL (eBioscience) was added during co-culture process when required. $CD8^+$ T-cell proliferation was analyzed by FACS and determined by considering the proliferating $CD8^+$ T-cells those where CFSE staining had decreased compared to unstimulated $CD8^+$ T-cells.

BrdU proliferation assay

MOs were differentiated to DCs and TolDCs as described above and BrdU (APC BrdU Flow kit, BD Pharmingen) pulses were added to a final concentration of 10 μM at days 2 and 4. On days 3, 4 and 5 cells were harvested and 10^6 cells were prepared for flow cytometry as described by the manufacturer. In brief, cells were fixed for 30 minutes on ice, permeabilized for 5 minutes on ice and

treated with DNAse for 1 h at 37°C to expose incorporated BrdU. Cells were then stained with fluorescent anti-BrdU antibody for 20 minutes at room temperature and analyzed in a BD FACSCanto-II flow cytometer. The HAFTL pre-B cell line was used as control for proliferation.

Flow cytometry

For the study of surface cell markers, cells were harvested after differentiation culture and washed once with PBS. Cell staining was performed in a staining buffer (PBS with 4% fetal bovine serum and 0.4% EDTA) after blocking for non-specific binding with Fc block (BD Pharmingen) for 5 minutes on ice. Cells were stained for 20 minutes on ice. Antibodies used included: CD14-FITC, CD80-PE, CD86-APC (Miltenyi biotec), CD11b-APC, CD1a-PE (Biolegend), HLA-DR-PeCy7 (eBioscience). Cells were also stained with the viability dye LIVE/DEAD™ Fixable Violet (Invitrogen) according to manuacturer's conditions. After staining, cells were fixed with PBS + 4% paraformaldehyde and analyzed in a BD FACSCanto-II flow cytometer in the following 48 h.

Cytokine measurements

For *in vitro* experiments, the concentration of IL-10 cytokine was measured from the cell culture supernatants using an enzyme-linked immunosorbent assay (ELISA), according to the manufacturer's instructions (BioLegend, San Diego, CA, USA). The concentration of IL-6 was measured with Beckman DXI Immunoassay analyzer using the access IL-6 reagent kit (Beckman Coulter) following the manufacturer's instructions.

Genomic DNA and total RNA extraction

DNA was extracted with a Maxwell RSC Cultured Cells DNA kit (Promega) following manufacturer's instructions. Similarly, total RNA was extracted with Maxwell RSC simplyRNA cells kit (Promega) following manufacturer's instructions.

Bisulfite (BS) and oxidative-bisulfite (oxBS) pyrosequencing

500 ng of genomic DNA was BS-converted with an EZ DNA Methylation-Gold kit (Zymo Research), following the manufacturer's instructions. The oxBS samples were purified via buffer exchange with Micro Bio-Spin® P-6 SSC columns (Bio-Rad Laboratories, Inc., USA) and eluted in ~22 μL MilliQ-water. After DNA denaturation with 1.25 μL NaOH (1M) for 30 min in a shaking incubator at 37°C, DNA was oxidized with 2 μL KRuO4 (15 mM) (Alfa Aesar, Germany) for 60 min in an ice-water bath (vortexing the reaction twice) and centrifuged at 16000 g for 15 min. Finally, oxidized DNA were BS converted using the EZ DNA Methylation™ kit (Zymo Research, CA, USA). BS- and oxBS-treated DNA was PCR-amplified using IMMOLASE DNA polymerase kit (bioline). Primers were designed with PyroMark Assay Design 2.0 software (Qiagen) (see Table S3 for primer sequences). Finally, PCR amplicons were pyrosequenced with the PyroMark Q24 system and analyzed with PyroMark Q48 Autoprep (Qiagen). 5mC levels were derived from the oxBS data, while 5hmC levels were calculated by subtracting the oxBS values from the BS values (5mC+5hmC) using the same biological replicate, as described in (Garcia-Gomez et al., 2017).

Real-time quantitative Polymerase Chain Reaction (RT-qPCR)

250 ng of total RNA were converted to cDNA with Transcriptor First Strand cDNA Synthesis Kit (Roche) following manufacturer's instructions. RT-qPCR primers were designed with Primer3 software (Koressaar and Remm, 2007) (see Table S3). RT-qPCR reactions were prepared with LightCycler® 480 SYBR Green I Master (Roche) according to manufacturer's instructions and analyzed with a LightCycler® 480 instrument (Roche).

Western blot

Protein expression and downregulation was visualized by western blotting, performed using standard Western blot. The following antibodies were used for Western blotting and Co-immunoprecipitation: Anti-Vitamin D3 Receptor (Cell Signaling), anti-TET2 (Abcam), anti-pStat3 (Fluidigm), anti-Stat3 (Cell Signaling Technology), anti-pStat1 (Cell Signaling Technology), anti-Stat1 (Cell Signaling Technology), anti-pStat5 (Fluidigm), anti-Stat5 (Thermo Fisher Scientific), anti-Lamin B1 (Abcam), anti-aTubulin (Sigma-Aldrich). anti-rabbit IgGs (Merck Millipore) and anti-mouse IgGs (Merck Millipore).

Co-immunoprecipitation (Co-IP)

Co-IP assays were performed using TolDCs differentiated from CD14 + monocytes for 3 days. Cell extracts were prepared in lysis buffer [50 mM Tris–HCl, pH 7.5, 1 mM EDTA, 150 mM NaCl, 1% Triton-X-100, protease inhibitor cocktail (cOmplete™, Merck)] with corresponding units of Benzonase (Sigma) and incubated at 4°C for 4 h. 100 μL of supernatant was saved as input and diluted with 2× Laemmli sample buffer (5x SDS, 20% glycerol, 1M Tris–HCl (pH 8.1)). Supernatant was first incubated with PureProteome™ Protein A/G agarose suspension (Merck Millipore) for 1 h to remove background signal. The lysate was then incubated overnight at 4°C with respective crosslinked primary antibody. The cross-linking was performed in 20 mM dimethyl pimelimidate (DMP) (Pierce, Thermo Fisher Scientific, MA, USA) dissolved in 0.2 M sodium borate (pH 9.0). Subsequently, the beats were quenched with 0,2M of ethanolamine (pH 8.0) and resuspended at 4°C in PBS until use. Beads were then washed three times with lysis buffer at 4°C. Sample elution was done by acidification using a buffer containing 0.2 M glycine (pH 2.3) and diluted with 2× Laemmli. Samples and inputs were denatured at 95°C in the presence of 1% β-mercaptoethanol.

DNA methylation profiling

Infinium MethylationEPIC BeadChip (Illumina, Inc., San Diego, CA, USA) arrays were used to analyze DNA methylation. This platform allows >850,000 methylation sites per sample to be interrogated at single-nucleotide resolution, covering 99% of the reference sequence (RefSeq) genes. The samples were bisulfite-converted using EZ DNA Methylation-Gold™ Kit (Zymo Research, Irvine, CA, USA) and were hybridized in the array following the manufacturer's instructions. Image processing and intensity data extraction software and procedures were as previously described (Bibikova et al., 2006). Each methylation data point was obtained from a combination of the Cy3 and Cy5 fluorescent intensities from the methylated and unmethylated alleles. Background intensity computed from a set of negative controls was subtracted from each data point. For representation and further analysis, we used beta and M values. The beta value is the ratio of the methylated probe intensity to the overall intensity (the sum of the methylated and unmethylated probe intensities). It can take a value between 0 and 1, and was used to derive heatmaps and to compare DNA methylation percentages from bisulfite-pyrosequencing experiments. The M value is calculated as the $\log_2$ ratio of the intensities of the methylated versus unmethylated probes. For the purpose of statistical analysis, M values are more suitable because they are normally distributed.

Raw methylation data were preprocessed with the minfi package (Aryee et al., 2014). Data quality was assessed using the minfi and RnBeads packages (Aryee et al., 2014; Assenov et al., 2014; Müller et al., 2019). After Snoob normalization, data were analyzed using aneBayes moderate t test available in the limma package (Ritchie et al., 2015). Several criteria have been proposed as representing significant differences in methylated CpGs, but in this study we considered a probe to be differentially methylated if it had a methylation differential of 20% and if it was significant ($q < 0.05$).

ChIP-seq analysis

Chromatin immunoprecipitation was performed using the iDeal ChIP-seq kit for Transcription Factors (Diagenode), according to the manufacturer's instructions. Briefly, cells on day 3 of differentiation were cross-linked with 1% formaldehyde for 15 min and glycine was added to quench the reaction (final concentration 125 mM, incubated for 5 min at room temperature). Cells were washed once with cold PBS, scraped off the plates, and pelleted. To obtain a soluble chromatin extract, cells were resuspended in 1 mL LB1 (50 mM HEPES, 140 mM NaCl, 1 mM EDTA, 10% glycerol, 0.5% NP-40, 0.25% Triton X-100 and 1× complete protease inhibitor) and incubated while rotating at 4°C for 10 min. Samples were centrifuged, resuspended in 1 mL LB2 (10 mM Tris-HCl pH 8.0, 200 mM NaCl, 1 mM EDTA, 0.5 mM EGTA and 1× complete protease inhibitor) and incubated while rotating at 4°C for 10 min. Finally, samples were centrifuged, resuspended in 1 mL LB3 (10 mM Tris-HCl pH 8.0, 100 mM NaCl, 1 mM EDTA, 0.5 mM EGTA, 0.1% sodium deoxycholate, 0.5% *N*-lauroylsarcosine, 1% Triton X-100 and 1× complete protease inhibitor). Chromatin extracts were sonicated for 12.5 min using a Covaris M220 focused ultrasonicator at a peak power of 75, and a duty factor of 10 and 200 cycles per burst. The lysates were incubated with anti-VDR antibody (12,550, Cell Signaling) bound to 30 μL protein A or protein G Dynabeads and incubated overnight at 4°C, keeping 5% as input DNA. Magnetic beads were sequentially washed with low-salt buffer (150 mM NaCl, 0.1% SDS, 1% Triton X-100, 1 mM EDTA and 50 mM Tris-HCl), high-salt buffer (500 mM NaCl, 0.1% SDS, 1% Triton X-100, 1 mM EDTA and 50 mM Tris-HCl), LiCl buffer (150 mM LiCl, 0.5% sodium deoxycholate, 0.1% SDS, 1% Nonidet P-40, 1 mM EDTA and 50 mM Tris-HCl) and TE buffer (1 mM EDTA and 10 mM Tris-HCl). For ChIP-seq, beads were resuspended in elution buffer (1% SDS, 50 mM Tris-HCl pH 8.0, 10 mM EDTA and 200 mM NaCl) and incubated for 30 min at 65°C. After centrifugation, the eluate was reverse-cross-linked overnight at 65°C. The eluate was then treated with RNaseA for 1 h at 37°C and with Proteinase K (Roche) for 1 h at 55°C and the DNA was recovered using a Qiagen PCR purification kit.

Sequencing reads from ChIP-seq experiments were mapped to the hg19 assembly of human reference genome using Bowtie2 Aligner v2.2.6 (Langmead and Salzberg, 2012). After removing reads with MAPQ < 30 with Sequence Alignment/Map (SAMtools) v1.2 (Li et al., 2009), PCR duplicates were eliminated using the Picard function available in MarkDuplicates software v1.126. Peak calling was determined using SPP (with parameters –npeak=300000 –savr –savp -rf). The irreproducible discovery rate (IDR) was used to filter peaks (IDR < 0.05). To visualize individual ChIP-seq data on Integrative Genomics Viewer (IGV), we converted bam output files to normalized bigwig format using the bamCoverage function in deepTools (v2.0).

ChIP-qPCR

ChIP assays were performed as previously described (Li et al., 2020). Briefly, MOs, DCs and TolDCs were crosslinked with 1% methanol-free formaldehyde (Thermo Fisher) for 15 min and subjected to immunoprecipitation after sonication. ChIP experiments were performed using the LowCell# ChIP kit™ protein A (Diagenode, Liège, Belgium). We used antibodies against vitamin D3 Receptor (Cell Signaling), acetylated H3 (H3ac), trimethylated lysine 27 of histone H3 (H3K4me3Millipore) and trimethylated lysine 4 of histone H3. Corresponding rabbit IgG (Diagenode) is used as control. Protein binding was analyzed by real-time quantitative PCR, and data are represented as ratio of the enriched fraction with respect to input. ChIP primers were designed for the areas flanking differentially methylated CpGs and their sequences are shown in Table S3.

Microarray reanalysis

Affymetrix datasets from human monocytes, and from *in vitro*- and *in-vivo* DCs and MACs were obtained from GSE40484 (Segura et al., 2013) and GSE102046 (Goudot et al., 2017). Affymetrix raw data from MOs, DCs and TolDCs were obtained from GSE13762 (Széles et al., 2009). Affymetrix raw data files were normalized by the robust multiarray average (RMA) algorithm and summarized,

after background correction, using the R package oligo (Carvalho and Irizarry, 2010). Normalized expression datasets were then merged and corrected for batch effects using ComBat function of the sva package. Finally, t-Distributed Stochastic Neighbor Embedding (tSNE) of 1000 most variant genes was performed in R using Rtsne package.

Data analysis

Hierarchical clustering was carried out based on Pearson correlation distances and average linkage criteria. For low-dimensional analysis, we used principal component analysis (PCA). Transcription-factor motifs were enriched for each set using HOMER software v4.10.3. Specifically, we used the findMotifsGenome.pl algorithm (with parameters -size 200 -cpg) to search for significant enrichment against a background sequence adjusted to have similar CpG and GC contents. Genomic regions for genetic context location were annotated using the annotatePeaks.pl algorithm in the HOMER v4.10.3 software application (Heinz et al., 2010). To determine the location relative to a CpG island (CGI), we used 'hg19_cpgs' annotation in the annotatr v1.8 R package. GREAT software (McLean et al., 2010) was used to enrich downstream pathways and gene ontologies. We used the single nearest gene option to identify associations between genomic regions and genes. Chromatin state analysis for DCs were assessed using the EpiAnnotator R package (Pageaud et al., 2018). Inference of TF activities from expression values were calculated using DoRothEA (Garcia-Alonso et al., 2019). We used the nichenetr package (Browaeys et al., 2020) to predict ligand activity.

QUANTIFICATION AND STATISTICAL ANALYSIS

All statistical analyses were done in R v3.5.1. Data distributions were tested for normality. Normally distributed data were tested using two-tailed unpaired Student's t-tests; non-normal data were analyzed with the appropriate non-parametric statistical test. Levels of significance are indicated as: *, $P < 0.05$; **, $P < 0.01$; ***, $P < 0.001$; ****, $P < 0.0001$. Non-significance ($P \geq 0.05$) is indicated as 'ns'.

Cell Reports, Volume *38*

Supplemental information

Vitamin D receptor, STAT3, and TET2 cooperate to establish tolerogenesis

Francesc Català-Moll, Anna G. Ferreté-Bonastre, Gerard Godoy-Tena, Octavio Morante-Palacios, Laura Ciudad, Laura Barberà, Federico Fondelli, Eva M. Martínez-Cáceres, Javier Rodríguez-Ubreva, Tianlu Li, and Esteban Ballestar

Figure S1

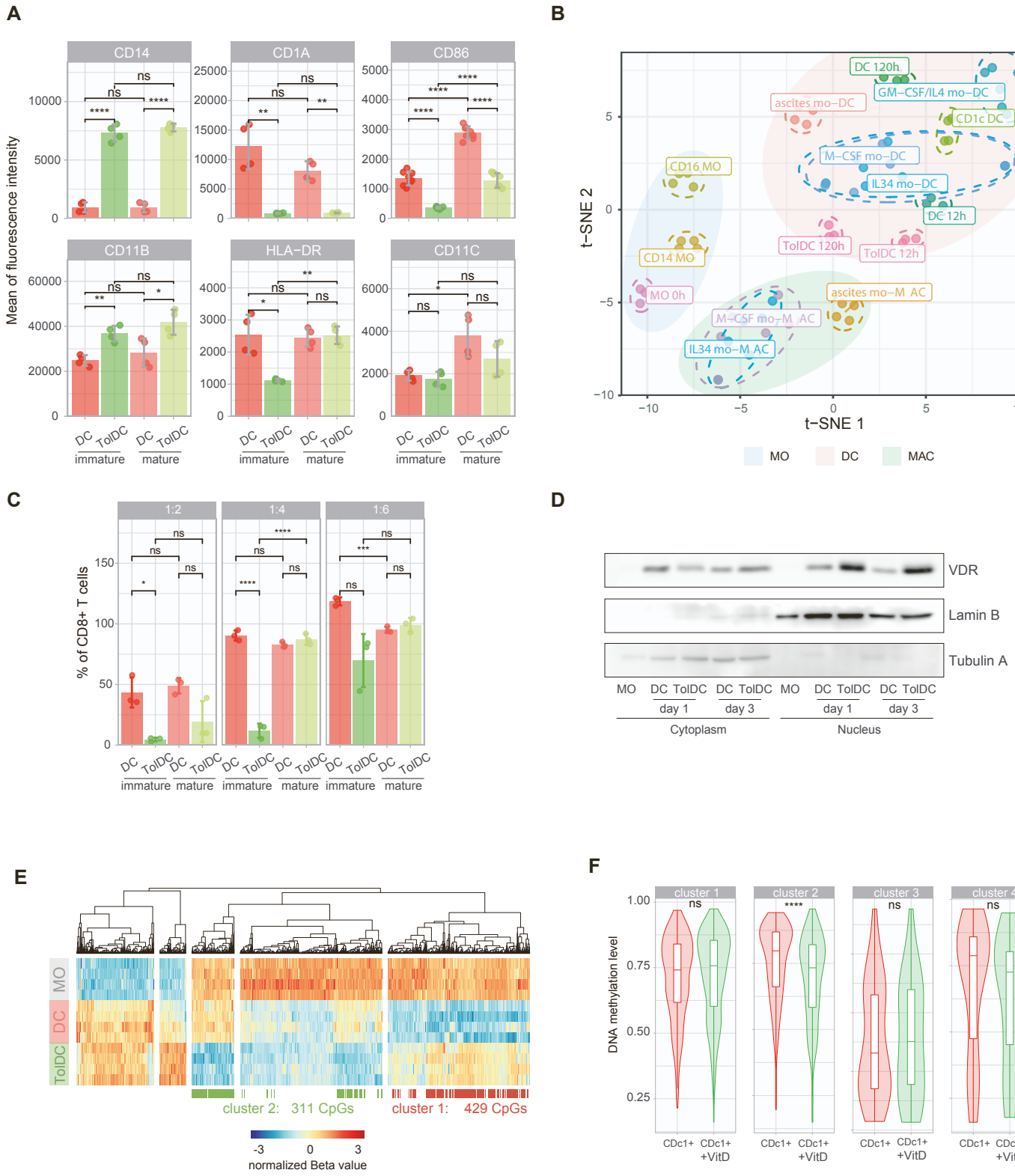
A
CD14
CD1A
CD86
CD11B
HLA-DR
CD11C
Mean of fluorescence intensity
DC
TolDC
immature
mature
B
DC 120h
GM-CSF/IL4 mo-DC
ascites mo-DC
CD1c DC
M-CSF mo-DC
CD16 MO
IL34 mo-DC
DC 12h
TolDC 120h
TolDC 12h
CD14 MO
MO 0h
ascites mo-M AC
M-CSF mo-M AC
IL34 mo-M AC
t-SNE 1
t-SNE 2
MO
DC
MAC
C
1:2
1:4
1:6
% of CD8+ T cells
D
VDR
Lamin B
Tubulin A
MO
DC TolDC DC TolDC MO DC TolDC DC TolDC
day 1
day 3
Cytoplasm
Nucleus
E
MO
DC
TolDC
cluster 2: 311 CpGs
cluster 1: 429 CpGs
-3
0
3
normalized Beta value
F
cluster 1
cluster 2
cluster 3
cluster 4
DNA methylation level
CDc1+
CDc1+ +VitD

Figure S1. **Characterization of DCs and TolDCs, Related to Figure 1** (**A**) Analysis of DC and TolDC surface markers by flow cytometry with (mature) and without (immature) LPS activation (n = 4, two independent experiments) in differentiated DCs and TolDCs. (**B**) t-Distributed Stochastic Neighbor Embedding (tSNE) analysis of 1000 most variable genes. Publicly available gene expression data (Goudot et al, 2017; Széles et al, 2009; Segura et al, 2013) of various subpopulations of monocytes (MOs), macrophages (MACs) and dendritic cells (DCs) were integrated as described in Methods. This analysis included mo-MACs and mo-DCs obtained from ascites (ascites-mo-MAC, ascite-mo-DC) (**C**) *In vitro* proliferation assay of allogeneic CD8+ T cells co-cultured with DCs and TolDCs at ratios of 1:2, 1:4 and 1:6 before (immature) and after (mature) LPS activation. CD8+ T cell proliferation as analyzed by flow cytometry utilizing CFSE staining (n = 4, two independent experiments). (**D**) Representative western blot assays showing levels of vitamin D receptor in cytoplasm and nucleus of MO, DCs and TolDCs at different time points of differentiation. Tubulin A and Lamin B were used as cytoplasmic and nuclear markers respectively. (n=3, one experiment) (**E**) Heatmap showing DNA methylation levels of four paired samples of MOs and their derived DCs and TolDCs. The heatmap includes all CpG-containing probes displaying significant methylation changes (differential of beta value >= 0.2 & q-value < 0.05) in all of three possible comparisons (DC-MO, TolDC-MO and TolDC -DC). The color annotation marks the membership to cluster 1 (DC-specific DNA demethylation) or cluster 2 (TolDC-specific DNA demethylation) as defined in Figure 1C (n=4, two independent experiments). (**F**) Box and violin plot representation of DNA methylation levels from *in vivo* circulating DCs (CD1c+ DCs) cultured *in vitro* for 48h with or without Vitamin D (VitD and DC, respectively). CpGs shown are classified in four clusters as defined in Figure 1C,D. Statistical significance in A and C was calculated using Student's t-test (* p-value <0.05, ** p-value < 0.01, *** p-value < 0.001, **** p-value < 0.00001).

Figure S2

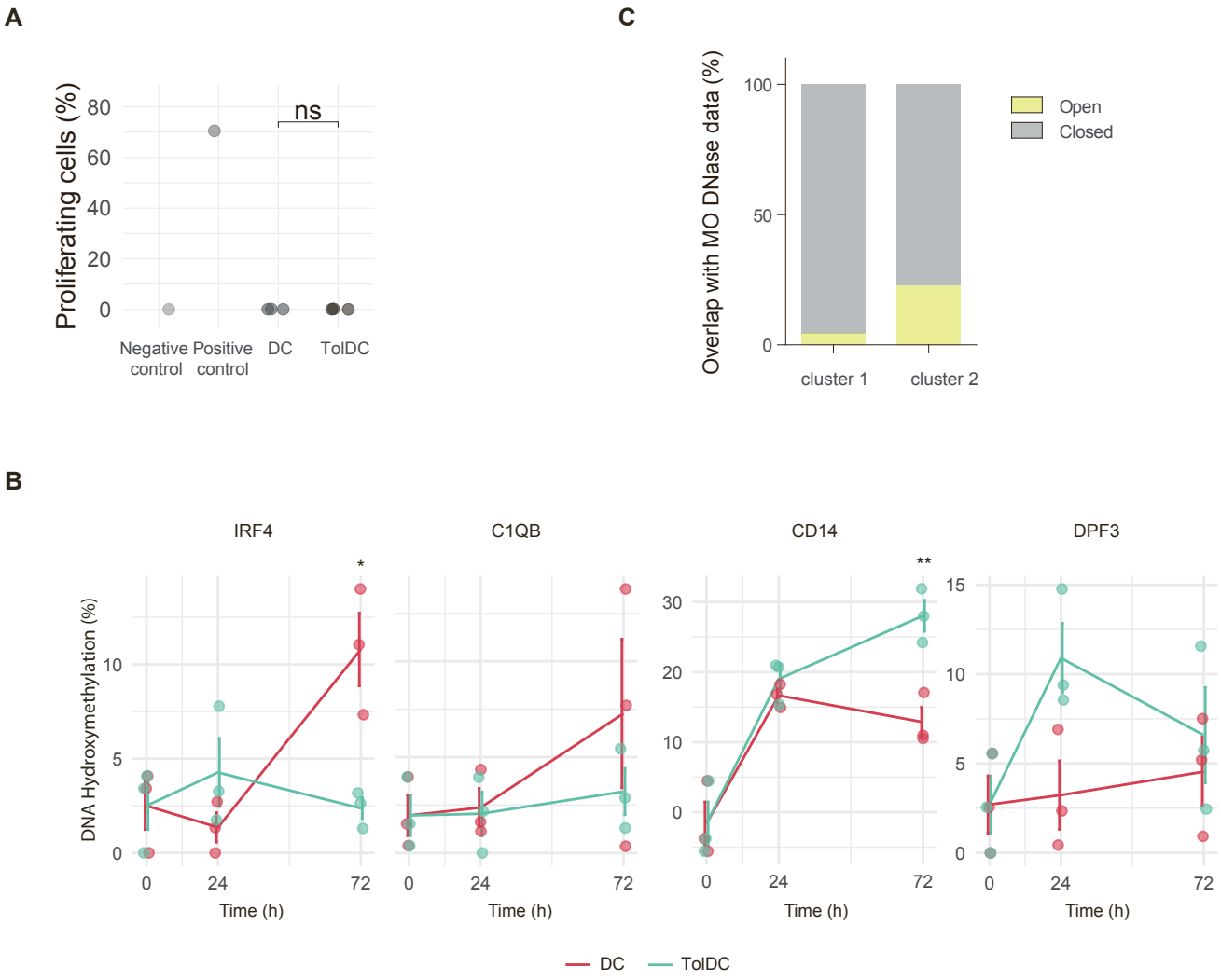
A
Proliferating cells (%)
80
60
40
20
0
ns
Negative control
Positive control
DC
TolDC
C
Overlap with MO DNase data (%)
100
50
0
cluster 1
cluster 2
Open
Closed
B
IRF4
C1QB
CD14
DPF3
DNA Hydroxymethylation (%)
*
**
Time (h)
0
24
72
DC
TolDC

Figure S2. **DNA methylation dynamics during differentiation to TolDCs, Related to Figure 2.** (**A**) Dot plot showing the results of a BrdU proliferation assay for the DCs and TolDCs differentiation model at day 5 (n = 3, one experiment). HAFTL cell line was used as a control. (**B**) Dot plot representation of 5hmC levels of two representative CpGs from cluster 1 (top) and 2 (bottom) at 24h and 72h of differentiation to DCs and TolDCs. Statistical test: unpaired two-tailed t-test (* p-value < 0.05, ** p-value < 0.01) (n=3, one experiment). (**C**) Bar plot representation of the chromatin accessibility state of the CpGs from cluster 1 and 2. Chromatin accessibility data was obtained from a DNase dataset from MOs.

Figure S3

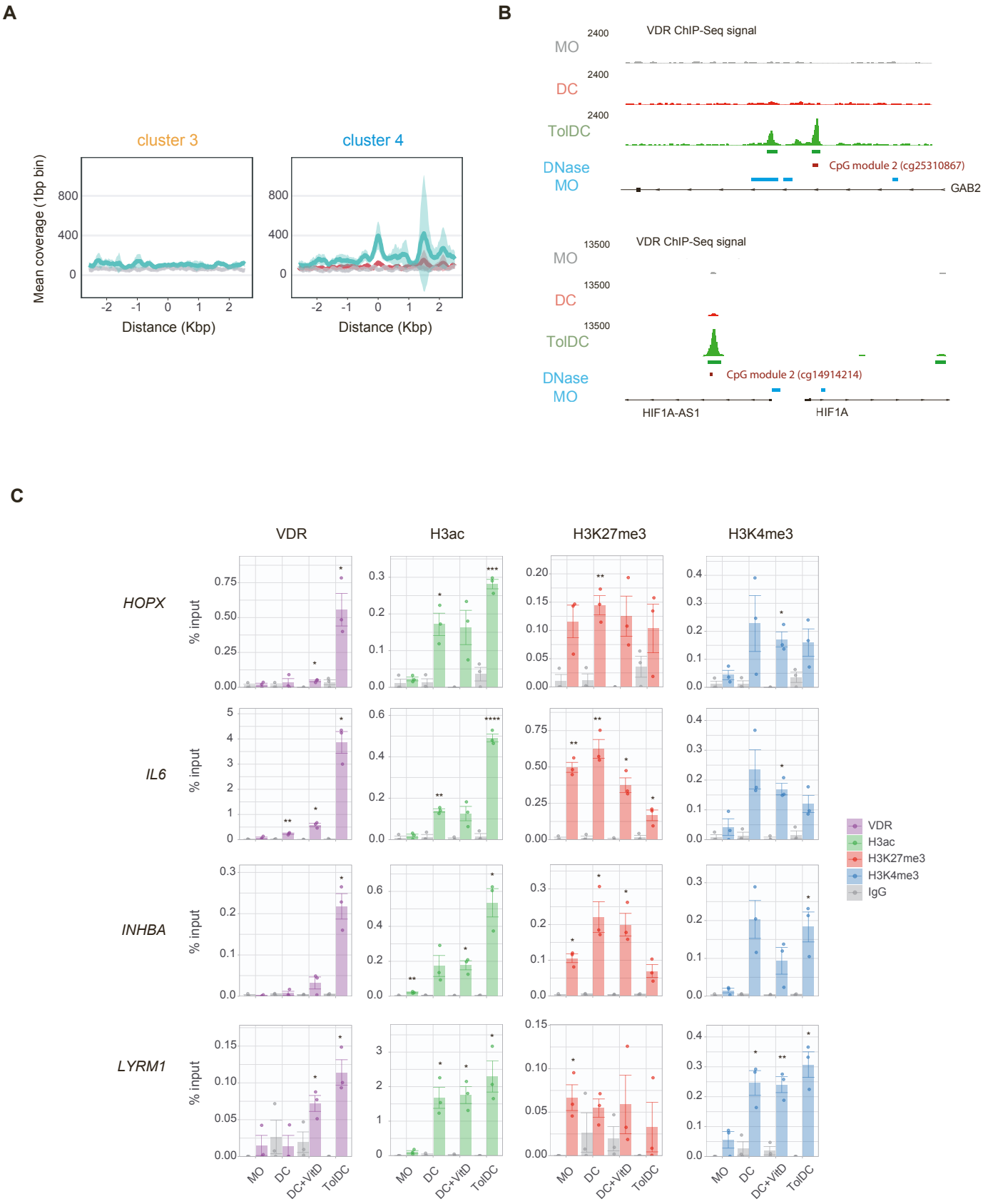
A
cluster 3
cluster 4
Mean coverage (1bp bin)
800
400
0
-2 -1 0 1 2
Distance (Kbp)
B
VDR ChIP-Seq signal
MO
DC
TolDC
DNase
MO
2400
CpG module 2 (cg25310867)
GAB2
13500
CpG module 2 (cg14914214)
HIF1A-AS1
HIF1A
C
VDR
H3ac
H3K27me3
H3K4me3
HOPX
IL6
INHBA
LYRM1
% input
MO
DC
DC+VitD
TolDC
IgG

Figure S3. Schemes zooming at TolDC-demethylated genes with VDR peaks, Related to Figure 4. (**A**) Composite plots of VDR ChIP-seq distribution ± 2.5 Kbp around CpGs from cluster 3 (left) and cluster 4 (right) in MO (grey), DC (red) and TolDC (green). Smooth represents the confidence intervals (CIs). (n=2, one experiment) (**B**) VDR ChIP-seq signal profiles in the vicinity of the representative genes with CpGs of cluster 2. VDR signals are colored by cell type. At the bottom, the significant VDR binding sites are shown in green, CpG position is depicted below in red DNase significant peaks in MOs are colored in blue. (**C**) Bar plot representation of ChIP-qPCR results for VDR binding and three histone modifications (H3ac, H3K27me3 and H3K4me4) in the vicinity of VDR peaks close to *HOPX, IL6, INHB* and *LYRM1* gene sequences. This analysis was performed in MO, DC and TolDC and DC+VitD, which consist of adding vitamin D for 30 min at the end of a 6-day differentiation to DCs. Immunoprecipitation with IgG was used as control. (n=3, one single experiment) Statistical test: unpaired two-tailed t-test (* p-value < 0.05, ** p-value < 0.01, *** p-value < 0.001, **** p-value < 0.0001).

Figure S4

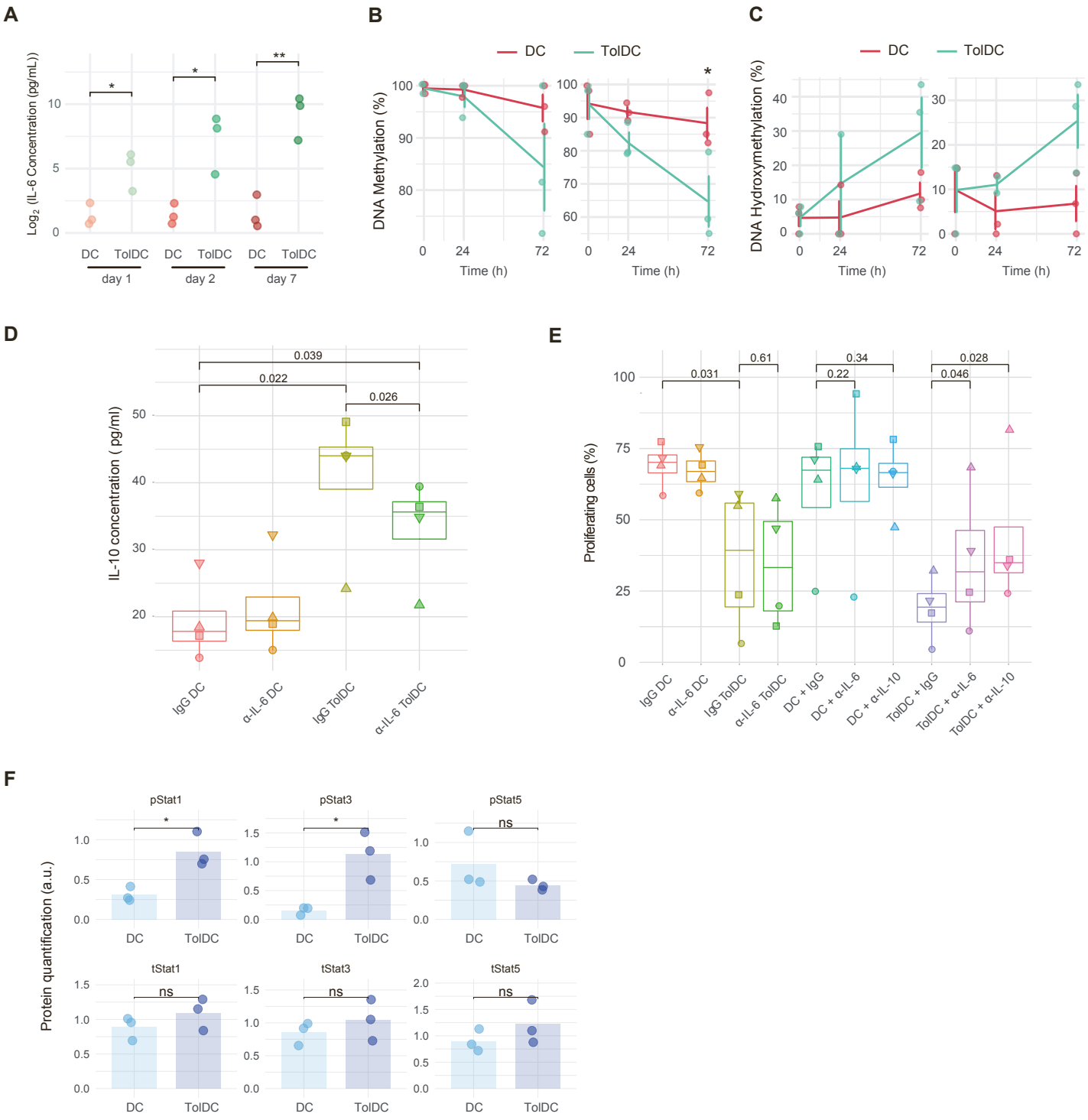
A
B
C
D
E
F
DC
TolDC
day 1
day 2
day 7
Time (h)
DNA Methylation (%)
DNA Hydroxymethylation (%)
IL-10 concentration (pg/ml)
Proliferating cells (%)
IgG DC
α-IL-6 DC
IgG TolDC
α-IL-6 TolDC
DC + IgG
DC + α-IL-6
DC + α-IL-10
TolDC + IgG
TolDC + α-IL-6
TolDC + α-IL-10
Protein quantification (a.u.)
pStat1
pStat3
pStat5
tStat1
tStat3
tStat5
ns

Figure S4. Activation of the IL-6/JAK2/STAT3 pathway in TolDCs, Related to Figure 5. (**A**) Dot plot representation of IL-6 secretion to the medium by DC and TolDC at day 1, 3 and 7 of differentiation (n = 3, one single experiment). **(B-C)** Dot plots representing DNA methylation levels (**B**) and DNA hydroxymethylation levels (**C**) of upstream regions of *IL6* gene on DC and TolDCs at 24h and 72h of differentiation (n=3, one single experiment). CpGs studied are cg02979021 (left) and cg07816106 (right). (**D**) Dot and box plot representation of the effect of the presence α-IL-6 antibody during the differentiation of DC or TolDC on IL-10 secretion to the medium. Each biological replicate is distinctly represented with a different shape. (n=4, one single experiment) (**E**) Dot and box plot representation of the effect on CD8+ proliferation of DC and TolDC in the presence of blocking antibodies against IL-6 or IL-10, and isotype IgG was used as a control. IgG DC and IgG TolDC, were differentiated in the presence of either IgG and samples α-IL-6 DC and α-IL-6 TolDC were differentiated in the presence of anti-IL-6. The samples DC + IgG, TolDC + IgG, DC + α-IL-6, TolDC + α-IL-6, DC + α-IL-10, TolDC + α-IL-10 were differentiated in the absence of any antibody; IgG, α-IL-6 or α-IL10 antibodies were added during the proliferation assay, respectively. Each biological replicate is distinctly represented with a different shape (n=4, two independent experiments) (**F**) Dot and bar plot representation of STAT1/STAT3/STAT5 protein quantification by Western Blot of DCs and TolDCs (n=3).

Figure S5

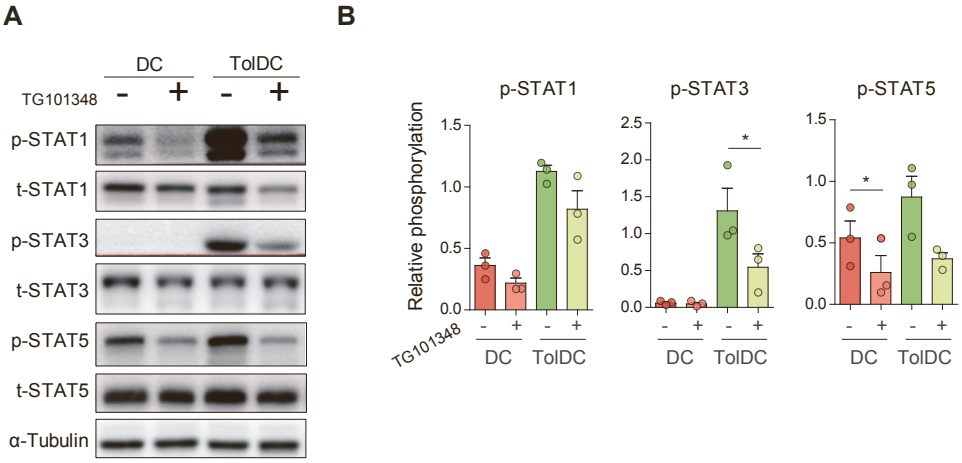
A
DC
TolDC
TG101348
- + - +
p-STAT1
t-STAT1
p-STAT3
t-STAT3
p-STAT5
t-STAT5
α-Tubulin
B
p-STAT1
p-STAT3
p-STAT5
Relative phosphorylation
1.5
1.0
0.5
0.0
2.5
2.0
1.5
1.0
0.5
0.0
*
*
TG101348
- + - +
DC TolDC

Figure S5. Specific inhibition of STAT3 phosphorylation reverts immunosuppressive properties of vitamin D exposed dendritic cells, Related to Figure 6. (**A**) Representative Western Blot showing the effect of TG101348 at the phosphorylation level of STAT1, STAT3 and STAT5 in DCs and TolDCs. (**B**) Bar and dot plot showing the proportion of phosphorylated STAT1, STAT3 and STAT5 as measured by Western Blot with or without TG101348 (n = 3, two independent experiments).